USING POISSON STATISTICS TO ANALYZE SUPERNOVA REMNANT EMISSION IN THE LOW COUNTS X-RAY REGIME

by

Quentin Jeffrey Roper

A thesis submitted in partial fulfillment of the
requirements for the Doctor of Philosophy
degree in Physics
in the Graduate College of
The University of Iowa

August 2014

Thesis Supervisor: Professor Randall L. McEntaffer

ProQuest LLC.
789 East Eisenhower Parkway
P.O. Box 1346
Ann Arbor, MI 48106 - 1346

Graduate College
The University of Iowa
Iowa City, Iowa

CERTIFICATE OF APPROVAL

PH.D. THESIS

This is to certify that the Ph.D. thesis of

Quentin Jeffrey Roper

has been approved by the Examining Committee for the thesis requirement for the Doctor of Philosophy degree in Physics at the August 2014 graduation.

Thesis Committee: _____
Randall McEntaffer, Thesis Supervisor

_____
Philip Kaaret

_____
Kenneth Gayley

_____
Cornelia Lang

_____
Rhonda DeCook

To my wife, for keeping me motivated in the most difficult of times.

Never ignore coincidence. Unless you're in a hurry, then always ignore coincidence.

The Doctor

ACKNOWLEDGEMENTS

I would like to acknowledge first and foremost the contribution of my wife, whose patience and understanding knows no bounds. Her insights and suggestions are manifold in this manuscript.

I would also like to recognize my advisor, Randall McEntaffer, who has suffered through every draft of every paper I've ever written. He is a code-breaker for being able to tease out my meaning from otherwise opaque writing.

I would like to thank my parents, who never doubted me, even when I did.

I would like to recognize my colleagues for giving me their valuable opinions and experience. I wish them all the future success they deserve. In particular, I would like to acknowledge Tom Brantseg, Casey DeRoo, Ted Schultz, Thomas Rodgers, and James Tutt, for extremely valuable conversations and feedback.

I would also like to thank my thesis committee members, Philip Kaaret, Ken Gayley, Cornelia Lang, and Rhonda DeCook, who spent their time giving me valuable insight into the writing process. They were especially helpful in giving me advice in both composition and content.

ABSTRACT

I utilize a Poisson likelihood in a maximum likelihood statistical analysis to analyze X-ray spectrographic data. Specifically, I examine four extragalactic supernova remnants (SNR). In this study, I look at IKT 5 (SNR 0047-73.5), IKT 25 (SNR 0104-72.3), and DEM S 128 (SNR 0103-72.4) and IKT 18 (SNR 0057-7226), all of which reside in the irregular dwarf galaxy the Small Magellanic Cloud (SMC). IKT 5, DEM S 128, and IKT 25 have been designated as Type Ia in the literature due to their spectra and morphology. This is troublesome because of their asymmetry, a trait not usually associated with young Type Ia remnants in the Milky Way and the nearby Large Magellanic Cloud (LMC). I present *Chandra X-ray Observatory* data on these three remnants, and perform a maximum likelihood analysis on their spectra. I find that the X-ray emission is dominated by interactions with the interstellar medium. In spite of this, I find a significant Fe overabundance in all three remnants. Through examination of radio, optical, and infrared data, I conclude that these three remnants are likely not "classical" Type Ia SNR, but may be examples of so-called "prompt" Type Ia SNR. I detect potential point sources that may be members of the progenitor systems of both DEM S 128 and IKT 5, which could suggest a new subclass of prompt Type Ia SNR, Fe-rich CC remnants. In addition, I examine IKT 18. This remnant is positionally coincident with the LBV+WN binary system HD 5980. Due to an outburst in 1994, in which its V-band brightness changed by 3 magnitudes (corrsponding to an increase in luminosity by a factor of 16), HD 5980 was classified as a luminous

blue variable star. I find that IKT 18 is a standard core-collapse SNR with an over-abundance of Ne. I also find that HD 5980 has increased in flux by a factor of ~ 10, and its spectrum has transitioned from line-dominated to continuum-dominated. I attribute this peculiar increase in luminosity to an increase in wind-wind interaction due to orbital motion. Finally, I find IKT 18 to be phenomenologically unassociated with HD 5980.

TABLE OF CONTENTS

LIST OF TABLES

Table

LIST OF FIGURES

Figure

CHAPTER 1

INTRODUCTION

As stars expend their fuel, they can go through an electron degenerate phase of some sort. For example, a star with mass similar to our sun will eventually end its life as a White Dwarf, an inert ball of leftover stellar core that is unable to fuse heavier elements. For stars much more massive than the sun, with a lower limit of ~ 8 $M_\odot$[0] (Chevalier 2005), will fuse heavier elements in their cores until they reaches iron. Since iron has the highest binding energy per nucleon, it cannot be fused to produce a net gain in energy. While these two situations are radically different in many ways, they are not supported against collapse by thermal pressure. Instead, it is supported by what is popularly known as "electron degeneracy pressure", which is essentially the Pauli Exclusion Principle made manifest, wherein two electrons cannot occupy a single quantum state. This electron degenerate matter, however, only results in a completely stable solution in the nonrelativistic case. As more matter is added to these electron degenerate systems, the momentum increases until the electrons transition from the non-relativistic to the relativistic regime. The relativistic regime is fundamentally different– in the relativistic regime, electron degenerate matter is only stable up to a certain total mass of the system. This mass is called the Chandrasekhar mass, and has been found to be ~ 1.4 $M_\odot$. As the degenerate matter increases beyond this mass,

[0] $M_\odot$ is the mass of our sun, roughly 2×10^{30} kg and the subscript $\odot$ is used to refer to a property of the sun.

electron degeneracy pressure is insufficient to support the structure of the material, and it undergoes a runaway, releasing an enormous amount of energy, $\sim 10^{51}$ ergs[1]. This cataclysmic event is known as a supernova (SN) explosion.

These supernovae (SNe) come in two distinct flavors. Someone unfamiliar with the subject might expect them to be named "Type I" and "Type II". Unfortunately, that would not be quite convoluted enough. Indeed, there are Type I and Type II SNe, which are distinguished by their lack of optical Hydrogen Hα lines and the presence of Hα lines, respectively. These types of SNe have their own subtypes, with Type Ia based on its lack of optical He emission and presence of Si , Type Ib, which has He emission in the optical, as well as O, Mg and Ca, and Type Ic, which has no He emission, but also emits in the O, Mg, and Ca. Type II SNe are subtyped largely based on the decay of their lightcurves, with Type II-L SNe, which decay linearly with time, and Type-P SNe, which reach a plateau phase. There are also a myriad of specific subtypes of these subtypes as well. For further discussion of how the types of SNe were originally identified, see Smartt (2009).

However, these classifications are largely in terms of their optical spectra, which is how SNe were originally studied. But it turns out that this typing scheme is largely ancillary in terms of the progenitor system of the SNe themselves. Types Ib, Ic, and all Type II SNe are caused by the Fe core of a massive star, with at least ~ 8 M $_\odot$. The cores of such a star will gather Fe, which cannot fuse exothermically,

[1]To put this in perspective, this is about the amount of (bolometric) energy the sun will release over its entire 10 billion year lifetime

until the mass approaches the Chandrasekhar Mass limit, at which point it collapses, either into a neutron star or a black hole. Type Ia SNe, however, are thought to be the result of a white dwarf that accretes mass from a donor. It is currently unknown whether the accreting partner of this white dwarf is a main-sequence star (known as a singly-degenerate system) or another white dwarf (known as a doubly-degenerate system).

1.1 The Evolution of Supernova Remnants

The SN explosion results in the material of the progenitor being expelled at $\sim$ 10,000 km/s, which is much greater than the sound speed in the medium. This results in a shock front which sweeps up the circumstellar material and interstellar material around the progenitor system. The SNR is in the so-called "free expansion" phase when this swept up mass is much smaller than the ejecta mass of the progenitor. For this reason, this phase is sometimes called the "ejecta dominated" phase. The SNR stays in this phase for $\sim$ 500 years after the SN explosion, but this is dependent on the ambient ISM density, the ISM density profile, the explosion energy, and the mass of ejecta (Truelove & McKee 1999). The ejecta soon differentiates itself into a Hubble-like distribution, with $v \propto r$. The thermal pressure from the slowing shock onto the ejecta creates a secondary shock that gains strength and propagates inward relative to the outward-propagating forward shock (Chevalier 1982), called the "reverse shock". The reverse shock reheats the ejecta as it propagates inward. For the evolution of the forward and reverse shocks, see Figure 1.1 from Reynolds (2008). The upper blue line indicates the position of the forward-propagating shock front as a function of time,

and the lower blue line indicates the position of the reverse shock as a function of time.

As the mass of ISM swept up by the forward shock becomes more and more substantial, it plays a more important role in the SNR blast wave mechanics. Once it becomes comparable to the ejecta mass, the SNR undergoes a transition to an "energy"-conserving phase whose expansion rate is well-modelled by a self-similar solution. Formally, self-similar means that statistically, a system has a property that is approximately the same over all scales. In this context, the relevant self-similar parameter is dimensionless, and takes into account the input energy, E, the ambient medium density, ρ_0, the radius of the remnant R, and the time t. The only relevant solution of the form $R \propto t^{\lambda}$, where λ is dimensionless, holds that $E/\rho_0 \times R^5/t^2$ is a constant over all R and t in this phase. This phase of the SNR lifetime is known as the Sedov-Taylor[2] phase, and the SNR can stay in this phase for tens of thousands of years. In this phase, the shock velocity is of order 10^{2-3} km/s and $R \propto t^{2/5}$. In Figure 1.1, the red curve represents the "Sedov ratio", $m = \frac{vt}{R}$, which should transition from ~ 1 in the free expansion phase to 2/5 in the Sedov phase.

The transition from the Sedov-Taylor phase is marked by the increasing efficiency of radiative cooling into a phase during which the shock rapidly cools. This phase begins at ~ 30 kyr from the SN explosion, and the plasma of the SNR begins to stop acting like it is a single parcel of gas in thermal contact. In this phase, the

[2]Named after two scientists, Leonid Sedov and Sir Geoffrey Ingram Taylor, who both developed the solution to apply it to calculating atomic bomb test yields for opposite sides of the Cold War.

momentum of a parcel of the SNR shock wave's momentum is conserved, leading to an $R \propto t^{1/4}$ time evolution. The shock velocity of the SNR is only a few times that of the sound speed of the ISM, which is $\sim$ 10-20 km/s.

Eventually, after the shockwave has swept up $\gtrsim 10^2 M_{ej}$, the shockwave velocity transitions to less than the ISM sound speed, and the shock dissipates entirely. By this point, the SNR has ceased to be visible in the X-ray, and eventually, merges entirely with the ISM.

Supernova remnants occupy an auspicious place in the universe. Whereas stars largely form out of gas, and process that gas into heavier elements, it is largely up to SN explosions to provide the energy to redistribute that processed material back into the universe. The propagation of SNRs from their SN explosion, through their various stages, and their eventual merger is the way that this processed material is re-mixed into the ISM, in order to seed new gas clouds, which will in turn collapse to form a new population of stars.

Studying properties of SNR are important for a number of reasons. SNe provide the dominant mechanism for feedback of energy and matter in the evolution of the universe, and provide new material for stars being born. SNRs are also thought to be the source of much of the high energy cosmic rays (Koyama et al. 1995)[3].

[3]Also they make for really nice pictures, which is really nice when you're trying to sell people on your research for grants and whatnot

1.2 Core Collapse vs Type Ia

Nearly every type of SN explosion type discussed in the opening paragraphs is due to the collapse of the core of a massive star. This results in a remnant that is rich in nitrogen, oxygen, or neon (Da Silva 1993), although the degree to which this is true depends greatly on the mass and composition of the progenitor massive star. The only exception is that Type Ia SNe. As they progress into the remnant phase, the Type Ia SNR are dominated by iron in the emission line portion of their spectrum. Many years after the SN explosion, this dichotomy of composition is one of the only ways to type SN explosions after the fact.

In recent years, there has been a number of studies that attempt to characterize SNR by their morphology. One such study has shown a link between soft X-ray morphology and progenitor type. Lopez et al. (2011) performed a survey of young line-dominated Large Magellanic Cloud (LMC) and galactic SNR by analyzing the two dimensional multipole moments of surface brightness in the soft X-ray regime. When examining the quadrupole moment versus octupole moment, this population of SNR were divided into two groups. In this sample, Type Ia SNR have lower quadrupole and octupole moments, thus being the more symmetrical in shape, both circularly and bilaterally, than their CC cousins.

Similar to the LMC, the Small Magellanic Cloud (SMC) is a small dwarf galaxy gravitationally bound to our own Milky Way. Also like the LMC, the SMC is at high galactic latitude, so it is relatively unobscured by galactic absorbing material. The distance to the SMC is relatively well characterized at 61 $\pm$ 3 kPc (Hilditch et al.

2005). These factors make the Small Magellanic Cloud an ideal place for studying extragalactic populations of SNR.

A detailed study of 13 SNR in the Small Magellanic Cloud (SMC) using *XMM-Newton* was performed by van der Heyden et al. (2004) in which they typed these objects based on morphology and spectral properties. In particular, they group three remnants, IKT 25, DEM S 128, and IKT 5 as probable Type Ia candidates. Their spectra are dominated by a single broad peak around 1 keV with little else in the way of line emission. This broad peak could be associated with Fe-L shell emission arising from shock heated ejecta thus leading to the Type Ia designations. In addition, they are markedly different from other SMC SNR in morphology, being very asymmetric in the soft X-ray band, as opposed to other, more symmetric core-collapse (CC) SNR. SNR 0102-72.3 is a well studied CC remnant (Flanagan et al. 2004) yet is highly symmetric both circularly and bilaterally. Other CC remnants in van der Heyden et al. (2004) also show high degrees of symmetry, such as IKT 6 (SNR 0049-73.6) and IKT 23 (SNR 0103-72.6).

But this trend in the SMC is the oppposite of what Lopez et al. (2011) finds: Aren't CC-type remnants supposed to be the less-symmetric ones? If the typing of SMC SNR in van der Heyden et al. (2004) is correct, the Lopez et al. (2011) trend appears to be in stark contradiction to SMC remnants. On the other hand, the three previously mentioned Type Ia candidates are highly asymmetric thus displaying a morphological dichotomy in the SMC that is opposite to that found in the LMC or Milky Way. We present here a study aimed at providing further clarity to this

apparent contradiction through spectral and spatial analysis of *Chandra* data for these Type Ia candidates, IKT 25, DEM S 128, and IKT 5. Detailed spectral analysis will either provide new insight into these objects and challenge their classification, or confirm the *XMM-Newton* study, thus solidifying the curious difference between the SMC and its closest neighbors.

This apparent contradiction suggests a more fundamental set of questions. Can you type a SNR based solely on its (X-ray) morphology? Can we characterize the environmental effects of an SNR have on its morphology, and does this effect elucidate or obfuscate typification? To answer these questions, I need both imaging and spectroscopic data that are sufficiently high-resolution to use conventional X-ray plasma models and determine properties of the SNR with sufficient accuracy to type the SNR. Another goal of my investigation is to conglomerate data at multiple wavelengths in order to better understand these potential Type Ia SNR. Are they truly Type Ia remnants, with characteristic overabundance of iron, or is there some other explanation of their X-ray 1 keV spectral feature? To what extent can their multi-wavelength morphologies aid in determining their respective progenitor systems, if at all? What role do their environments play in determining their morphology? Does the environment of the remnant dominate morphology or does the ejecta? A part of my goal is to provide insight to these questions with regards to IKT 5, IKT 25 and DEM S 128, and ultimately shed light on the SNR morphology dichotomy.

1.3 Luminous Blue Variables

Luminous Blue Variable (LBV) stars are the largest of stars, thought to be greater than 50 $M_\odot$. These stars radiate near their Eddington luminosity, meaning that the gravity of the star is constantly fighting against the immense radiation of the star (Massey 2003). The most famous examples of these stars are η Carinae, and S Doradus. Occasionally, the radiation field wins, leading to the outer layer of the star being swept away by the radiation pressure of the star. During this time, the LBV puffs out, greatly increasing its radius until its outer envelop separates from the star. The resulting outburst can change the V-band magnitude of the star by $\gtrsim 2.5$ mag, an increase in nearly 10 times in luminosity. During these outbursts, the LBVs change in spectral type, after which time they tend to stabilize. Some of these LBV outbursts are so powerful, they are mistaken for SNe explosions. Such outbursts are referred to as "supernova imposters" (see, e.g. Chu et al. (2004)). However, while in principle similar to SNe, most LBV outbursts can be distinguished from SN explosions by their relatively low-velocity ejecta, which is at the escape velocity of the star, ~ 200 km/s, is much too low for a standard SN explosion until well into the remnant phase, and the amount of ejected material is also much smaller than that of a SNe, at ~ 0.2 $M_\odot$.

Soon after the LBV outburst, the star returns to its original, much smaller radius as it stabilizes. At this time, the star is giving off wind like a normal massive star, which can reach ~ 1600 km/s. The wind soon catches up with the outburst ejecta, and there is a discontinuity between the interface of this wind with the earlier outburst, forming an emission nebula capable of producing X-rays. This extended

gas complex around the LBV is called an LBV nebula.

1.4 Modelling optically thin plasmas in the X-ray

In the coronal approximation, we assume that the dominant heating mechanism of our plasma is collisional in nature. This means that we assume the main actors of this plasma are the electrons, and we assume that there is some characteristic temperature of the electrons that has a large effect on the heating dynamics. It should be noted that the ions may have their own characteristic temperatures, but because this plasma is not in local thermodynamic equilibrium, that temperature need not be (and in nearly all cases, is not) the same as the electron temperature. So when I refer to "temperature" in the following paragraphs, and in my fits in Section 3, I am referring to the temperature of the electrons. Even though we have assumed that the electrons are more important in the heating process, ions are incredibly important for providing the dominant cooling rate, as they provide these different modes for photon emission.

1.4.1 Continuum processes

Continuum processes start with a free electron. Since a free electron's energy is not quantized, all continuum processes tend to happen over a large range of energies. This is in contrast to discrete processes (discussed below), which involve bound electrons, whose energies are quantized. Thus the photons that are emitted through discrete processes have very specific energies, corresponding to the difference in the discrete energy states.

1.4.1.1 Radiative Recombination

Radiative Recombination is when an electron and an ion combine to form a new ion of the same element, whose net charge is one less than the original ion. When this happens, at least one photon is emitted whose total energy is equal to the change in energy between the free electron and the new ion formed.

It is possible for a free electron to recombine with an ion, in the process exciting another bound electron into a higher energy state, from which the ion will further decay. This phenomenon is known as dielectronic recombination. This situation can result in autoionization, wherein an electron is ejected from the ion, or radiative decay of two photons, one of which is a continuum photon, and the other which is a satellite line.

1.4.1.2 Thermal Bremmstrahlung

Thermal Bremmstrahlung, also known as "braking radiation" or free-free emission, is the process where an electron is deflected by an ion. The electron remains free, but is accelerated by the ion's electrostatic force to produce radiation, changing its velocity. A photon is emitted corresponding to the electron's change in kinetic energy.

The general equation governing the bremmstrahlung emission of a single particle with velocity v is given by

$$\frac{dW}{d\omega dV dt} = \frac{16\pi e^6}{3\sqrt{3}c^3 m^2 v} n_e n_i Z^2 G_{ff}(v,\omega) \tag{1.1}$$

where e and m are the charge and mass of the electron, Z is the charge of the

ion in units of electron charge, n_e and n_i are the number densities of electrons and ions. G_{ff} is a correction factor known as the gaunt factor.

In general, the spectral energy distribution of bremmstrahlung depends on the velocity distribution of the electron population. In a thermal population of electrons, this distribution is a Maxwell-Boltzmann distribution. The number of electrons at velocity v follows

$$dN \propto 4\pi v^2 e^{-mv^2/kT} dv \tag{1.2}$$

which yields the equation describing energy emitted due to thermal bremmstrahlung

$$\epsilon_\nu^{ff} \equiv \frac{dW}{d\nu dV dt}(T,\nu) \propto e^{\frac{-h\nu}{kT}} (kT)^{-1/2} Z^2 n_e n_i G_{ff,T} \tag{1.3}$$

1.4.2 Discrete Processes

Discrete emission processes arise when transitions are limited to specific energies. This only occurs when an ion in an excited state decays to a lower energy state. In general, this can happen in a few different ways. Energetic electron collisions can provide a method to excite an ion. Collisional excitation dominates as long as there is a sufficiently dense, sufficiently energetic population of free electrons, their collision with ions will dominate the excitation process. Recombining electrons can combine with the ion into an excited bound state. The flux of line emission follows the equation

$$F = \frac{\epsilon(T_e)}{4\pi R^2} \int n_e n_H dV \tag{1.4}$$

where ϵ is the line emissivity as a function of temperature, and R is the distance to the source.

1.5 Collisional Ionization Equilibrium

Collisional Ionization Equilibrium (CIE) is the regime in which the collisional heating rate and the radiative cooling rate are equal. This means that the rate of ionization and recombination are equal, i.e. that

$$\Gamma n_e n_{Z,z} = \alpha n_e n_{Z,z+1}, \tag{1.5}$$

where Γ and α are independent rate constants governing radiation and recombination, which may be temperature dependent, but do not depend explicitly on density. Z is a given element, and the ionization state z. This equality leads to a quasi-static distributions of ions across all elements, referred to as the ion balance.

In CIE, the excitation and de-excitation are also in equilibrium. The spectral energy distribution in this regime can be completely characterized by the temperature and density of the electrons, the densities of every ion species present, and the geometry of the plasma. This means that if we can estimate the number of collisions of electrons and each ion species in our plasma, we know that the spectral energy distribution is equal to the total emission from discrete and continuum contributions from this ion species.

Even in the case where a plasma is not in a CIE state, it is modelled in terms of the CIE plasma. You can imagine a case when electrons and ions are heated by some impulsive process, such as a shock, but are not in CIE. The continuum contributions to the plasma depend on electron collisions, and thus more or less immediately reflect

the changed electron temperature. However, the discrete contributions to the plasma have an ionization balance that reflects a different electron temperature. This is because the electrons and the ions have not come into CIE yet.

1.5.1 How plasma models are parametrized

Now that we have layed the framework on how we model collisional plasmas, we can explain how plasma models are calculated. We know that we need information about the density of ions, the density of electrons, as well as the temperature of electrons. With this information, we can completely characterize a plasma in CIE. This statement assumes that we know all of the relevant physics that goes into the emission processes, including all transitions that occur in every ion at every temperature. This is completely untrue, but great strides have been made over the last decade in both atomic simulations as well as laboratory data in augmenting our knowledge of the relevant atomic data (Brickhouse et al. 2009).

For a given element, if we know the ion balance as a function of electron temperature, the minimum information required is the number density of the electrons, the number density of each element, and the electron temperature. The number of electron-atom collisions per unit time that occur in a plasma in a volume V is

$$\int_V n_Z n_e dV \tag{1.6}$$

which is known as the partial emission measure of element Z with number density n_Z. However, X-ray plasma models are usually parametrized in a different way. As long as all such elements are distributed in the plasma the same way, one

can rewrite this equation as

$$A_Z \int_V n_H n_e dV, \tag{1.7}$$

where $A_Z \equiv n_Z/n_H$, which is referred to as the "abundance" of metal Z. Also, rather than using this ratio, the abundance is typically compared to the abundance of the sun, or the local solar environment. When I cite abundances in a model fit to a spectrum, I will frequently cite that abundance in terms of solar abundance, which is $A_Z/A_{Z_\odot}$. The other quantity, $\int_V n_H n_e dV$, is called the "total emission measure" of the plasma, or more usually abbreviated as simply the plasma's emission measure. In collisional ionization equilibrium, a thermal plasma's X-ray spectrum can be entirely characterized by the abundance table A_Z, the total emission measure, and the electron temperature T_e.

While the ionization parameter governs the power emitted by the plasma, the amount of flux recieved by a telescope on earth depends on the distance between the source and earth, D. So plasma models are parametrized in terms of the "norm" of the plasma,

$$norm_{thermal} = \frac{10^{-14}}{4\pi D^2} \int_V n_H n_e dV. \tag{1.8}$$

1.5.2 Collisional non-equilibrium

As mentioned above, a change in the plasma state, such a shock, is reflected in the relative changes from continuum and discrete processes. The discrete processes, as noted above, are determined by the ion balance, which depends on the electron temperature. The continuum emission also depends on the electron temperature. In CIE, the temperatures derived from these two sources are equal. However, in the

event of the electron temperature being impulsively changed (by, i.e. a supernova blast wave), the continuum emission and the discrete emission react over different timescales. The continuum emission component reacts, more or less, immediately, and moves to reflect the new temperature. However, the discrete component lags behind, as it takes some amount of time for the ions to realize that the temperature of the electrons has changed. In the case of SNR blast waves, the supersonic shock wave heats the medium impulsively. As the electrons collide with ions more often, the ionization rate begins to rise to reflect the higher electron temperature. This situation is known as a non-equilibrium ionizing (NEI) plasma, because the ionization rate of the plasma is higher than the recombination rate[4].

The ionization and recombination rates of an ion species are proportional to the electron density n_e, and is represented by the matrix equation

$$\frac{d\mathbf{F}}{dt} = n_e \mathbf{A} \cdot \mathbf{F}, \frac{d\mathbf{F}}{d\tau} = \mathbf{A} \cdot \mathbf{F}, \tag{1.9}$$

where $\mathbf{F}$ is a $Z+1$ length vector for the ionization "balance"[5] of the element Z, with the first component being the neutral form of the element, and the $Z+1$ component being the fully ionized form of the element. By construction, the sum of the components of $\mathbf{F}$ is unity. The matrix $\mathbf{A}$ is a tridiagonal matrix whose elements yield the

[4]Similarly, a plasma that cools works the same way, but instead the plasma's recombination rate is higher than its ionization rate. This is known as a non-equilibrium recombining plasma. Astrophysically, this is a somewhat more exotic plasma, and until recently, was not thought to occur in SNR. For a recent example where an SNR is thought to be in a recombining state, see Ohnishi et al. (2014)

[5]The quotations are to indicate that, of course, this varies with time because we are not in CIE.

probabilities of single-electron ionization, recombination, and remaining unchanged in charge[6]. The quantity $\tau \equiv n_e t$ is known as the ionization parameter, or sometimes the ionization timescale. The exact form of the solution of this matrix equation is outside of the scope of this thesis[7], but the important takeaway is that the matrix equation approaches a final ionization fraction at large values of ionization parameter, as you might expect as the system approaches CIE. However, each element approaches CIE at its own rate (Figure 1.2), but typical ionization parameters for NEI plasmas vary from $\sim 10^9$ s cm^{-3} to 10^{12} s cm^{-3}. Any larger than this range, and the plasma is essentially in CIE for all elements across all temperatures. Values less than this range are possible, but are seldom modelled because the ionization states are so low that they typically do not emit in the X-rays.

1.5.3 Derived physical characteristics

Using the parameters of these plasma models, one can calculate additional characteristics such as plasma density and shock velocity in order to learn more about these remnants and under what conditions they formed. The Rankine-Hugoniot jump conditions are a set of equations governing strong shocks. They are mathematical restatements that the mass, momentum and energy that passes across a shock have to exit the other side of the shock. Solving the Rankine-Hugoniot relations in the strong shock case with $\gamma = 5/3$ gives the post-shock temperature as a function of

[6]By assumption, this approach neglects the possibility of ionization resulting in the emission of two or more electrons from the atom, such as the Auger effect.

[7]For more information on the form of the solution, see Hughes & Helfand (1985)

shock velocity, $kT = (3/16)\mu m_p v^2$, with the average mass per particle $\mu = 0.6$. We assume that $T_e \sim T_{ion}$ as expected through Coulomb collisions in a plasma with a temperature of $\sim 10^6$ K and $n_e \sim 1$ cm^{-3} (Draine 2011)). If the electrons and ions are not in temperature equilibrium then the calculated velocities signify lower bounds. The density is found using the *norm* parameter for each component. A value of 61.3 kpc is used for D (Hilditch et al. 2005) and we assume that $n_e = 1.2 n_H$. We include a filling factor, f, which ranges from 0 to 1, to account for the fraction of the volume actually filled with X-ray emitting plasma. We can also estimate the age of the remnant from the equilibrium shock velocities. Assuming that each remnant is in the Sedov-Taylor phase, the time since shock heating can be calculated as $t = (2/5)R/v$, where R is the estimated shock distance from the center.

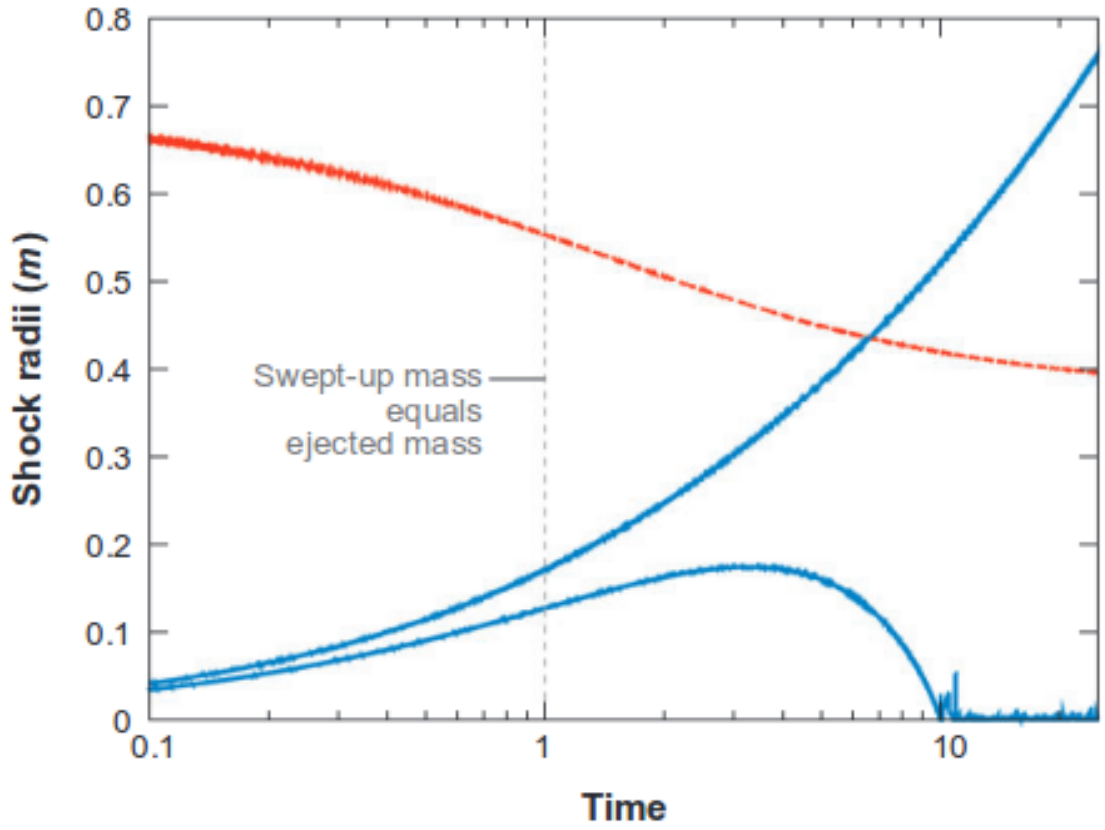

Figure 1.1. A hydrodynamic simulation of the SNR forward and reverse shock propogation as a function of time from Reynolds (2008). Time is in units of the Sedov-Taylor timescale, the amount of time the SN blast wave sweeps up an ISM mass equal to that of the ejecta. Shock radius is in arbitrary units. The upper blue line is the position of the forward propagating shock as a function of time, and the lower blue line is the position of the reverse shock as a function of time. The red line is the "Sedov ratio" $m = \frac{vt}{R}$, where R is the position of the forward shock, which transitions to 2/5 into the Sedov-Taylor phase. The dashed vertical line is the Sedov time, the time when the mass swept up by the blast wave equals the mass ejected from the SN explosion.

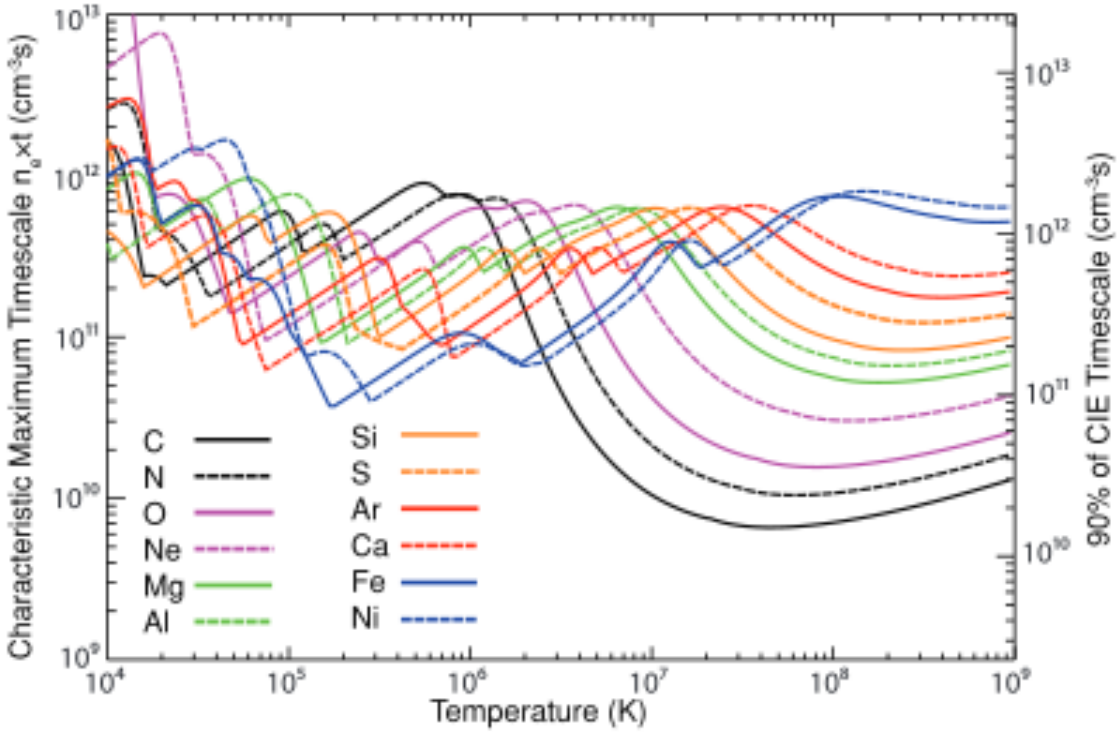

Figure 1.2. Characteristic ionization parameters over which a number of elements approach collisional ionization equilibrium as a function of temperature. In a plasma of the electron temperature, if a given element has an ionization parameter greater than that of the plot, $1/e$ (left axis) or 90% (right axis) of the population will be in CIE.

CHAPTER 2

STATISTICS APPLIED TO X-RAY SPECTROSCOPY

2.1 X-ray Stastistics in the Gaussian Regime

Rather than modeling "flux per spectral bin", as you might expect in other wavelengths, X-ray spectra tend to be modeled in terms of "counts per spectral bin", which takes a source spectral model and folds it through the detector responses. This is because the spectral response of X-ray telescopes acts as a transformation matrix $A(E, E')$, where E represents the energy of the incoming photon, and E' is the energy bin in which the photon is counted. In general, the response matrix A is noninvertable. This means that in general it is not possible to reconstruct a spectral energy distribution independent of how it is modelled. So rather, X-ray spectra are modeled through counts per spectral bin received by the detector.

Even though counts detected per spectral bin ought to follow a Poisson distribution, typical spectra are fit using a Gaussian distribution of counts per bin. This leads to the familiar χ^2 statistics. This is employed for a number of reasons. First off, in the limit of high count rates in every bin, the Central Limit Theorem guarantees that the number of counts per bin[1], in general a Poisson distribution, approaches a Gaussian distribution, so a χ^2 analysis is entirely appropriate. Secondly, because Gaussian distributions add and subtract from one another, it is trivial to take into account background spectral information. On a per-bin basis, simply subtract the

[1]In X-ray astrophysics, this is generally taken to be ~ 20 counts per bin, but there is no universally agreed upon standard of "enough counts"

mean background from the source+background spectrum to get the spectrum of the source without the background. The uncertainty is thus the quadrature sums of the uncertainties of the background and the source+background spectrum. Next, when employing a χ^2 analysis, it is easy (by eye) to evaluate the goodness-of-fit. In the limit of many degrees of freedom, the reduced χ^2 statistic, which is simply the χ^2 statistic divided by the number of degrees of freedom, should be ~ 1 for a good fit.

Goodness-of-fit is evaluated through χ^2_r, the reduced χ^2. This is simply the χ^2 statistic divided by the number of degrees of freedom, equal to the number of data points in the desired fit minus the number of model parameters $\theta_\mathbf{i}$ allowed to vary in the fit. For a "good" fit, this quantity should be near unity when The property that for a fit parameter $\theta_\mathbf{i}$ near its best fit value $\bar{\theta}_\mathbf{i}$.

Finding the confidence interval for $\bar{\theta}_\mathbf{i}$ is done by assuming that the likelihood goes like

$$\exp\left(\frac{(\bar{\theta}_\mathbf{i} - \theta_\mathbf{i})^2}{\sigma^2_{\theta_i}}\right) \tag{2.1}$$

near $\bar{\theta}_\mathbf{i}$. This makes calculating the confidence interval trivial, as evaluating the quantity $\sigma^2_{\theta_i}$ numerically is very easy to accomplish, provided that the model parameters are not correlated with one another. In addition, the likelihood ratio test can be used to test for additional model components in Gaussian statistics as well. In practice, the likelihood ratio test is often simplified to the simple F-test.

Unfortunately, χ^2 statistics is not appropriate for spectral modeling in which there are spectral bins containing few counts. This is a problem even with many bins with many counts, because the best fit obtained will be unduly biased towards the

low-count bins, and therefore unreliable. The common way of getting around this situation is to combine nearby energy bins until the counts spectrum has no bins with low counts. This comes with the drawback of effectively lowering the spectral resolution of the resultant spectrum. For an example of this, see Figure 2.1. The top panel of this figure shows the raw X-ray spectrum of the potential luminous blue variable star HD 5980. This spectrum has many bins with less than 20 counts, and a standard χ^2 statistical treatment of this object would have it rebinned with more than 20 counts per spectral bin, which we have displayed in the bottom panel. However, in doing this, the effective spectral resolution of the data has been reduced by a factor of ~ 5, which reduces the number of degrees of freedom in any resulting modelling, and essentially throws away spectral information.

2.2 The next step: Poisson Maximum Likelihood Analysis

A potential solution is to abandon the standard χ^2 statistical treatment for our analysis in spectra with spectral bins with less than 20 counts per bin. However, any potential replacement would have to offer the following: It would have to be completely valid in the limit of low count bins without compromising the data (like rebinning would do). We would have to be able to evaluate goodness-of-fit in some way. We would also have to be able to evaluate parameter confidence intervals in the resulting best fit.

We consider two potential solutions to this situation. The first is to abandon the Gaussian regime altogether, and make use of the Poisson distribution of counts in each bin and perform a Poisson maximum likelihood analysis. The Poisson Likelihood

function of a dataset D with predicted model M is of the form

$$\mathcal{L} = \prod_i \frac{M_i^{D_i}}{D_i} exp(-M_i) \tag{2.2}$$

where i is, for our purposes, a spectral bin.[1]In order to derive a statistic analogous to the χ^2 statistic in the Gaussian likelihood case, one can take the logarithm of the Poisson likelihood function, multiply it by negative two, and then drop all the terms that are only dependent on the dataset itself, which will not vary when optimizing the statistic, we come up with

$$\mathcal{C} = -2log(\mathcal{L}) = 2\sum_i (M_i - D_i log(M_i) \tag{2.3}$$

which can be minimized similarly to the χ^2 statistic.

The second method is to modify the uncertainty in each bin using the "Churazov" method as described in Churazov et al. (1996). This replaces the Poisson uncertainty of a low count bin with the Gaussian uncertainty derived from the binned spectrum with a minimum number of counts.

To test these two statistics against one another, simulations of a test spectrum are employed. In lieu of a more general test between these two statistics, I choose to test the different statistics based on a simulated spectrum. This parent X-ray spectrum must exhibit the properties we expect from remnants in the SMC. We therefore choose to model a spectral fit of a region of IKT 25, referred to as "Bar Region 1" from Lee et al. (2011) as our representative spectrum, with a Poisson noise component added. The statistic that best reproduces this parent spectrum should

[1]We note, although, that this is applicable to far more than the case of spectral modelling.

yield the most reliable results when utilized for our data. Each statistical method is used in Monte Carlo simulations to reproduce the parent spectrum. We compare the fit parameters derived from 10000 simulations using either the Cash (Poisson errors in each bin) or Churazov statistic (adjusted Gaussian errors in each bin) to the input, parent parameters. As in Lee et al. (2011), we allow four parameters to vary: the temperature, kT; the emission measure, $norm$; the iron abundance, Fe; and the ionization parameter, τ. The results are presented in Table 2.1. For each fit parameter, the simulated spectra using the Cash statistic with Poisson statistics more accurately reproduces the parent spectrum. We therefore, diverge from the Churazov fitting method used in Lee et al. (2011) and use a maximum likelihood analysis for our spectra.

With the Cash statistic chosen, we define a paradigm of evaluating goodness-of-fit. First, we identify the parameters of the best fit model to the spectrum. We then use this as a seed for the Sherpa task *fake_pha* to create simulated spectrum based on this model. We then compare a new fit to this simulated spectrum to the original, best fit of the actual spectrum. When performed many times (2000), this forms a distribution of simulated fit statistics that can be compared to the fit of the actual spectrum. If the original best fit model to the actual spectrum is an accurate representation, then the simulated fit statistics should be normally distributed about the original best fit model statistic. If this is not the case, then the original fit is not accurate. For our analysis, if the original fit statistic is contained within the 5 and 95 percentile levels of the simulated statistic distribution then the fit is considered

"good". As an example we simulate the expected histogram of statistics of the best fit models for two of our regions, region D and the Wisp from IKT 25. The result is shown in Figure 2.2. In these plots the vertical line is the statistic derived from the best fit to the spectrum while the histogram is the distribution of simulated fit statistics. The plot on the left displays a set of simulations that reproduce the best fit well. On the right the original best fit lies beyond the 95% limit and the model must be ruled out and the process starts over with a new model definition.

Now that we can rule out poor fits, another question we have to consider is how to measure the statistical significance of additional model parameters. If fitting the spectrum to a more complicated model yields a Cash statistic greater than or equal to that obtained by fitting to the simpler model, it can clearly be ruled out in favor of the simpler model. In the case of a lower Cash statistic we again utilize Monte Carlo simulations similar to those above. We begin by determining the best fit to the spectrum obtained using the additional parameter. We then simulate spectra many times using the best fit model derived from the simpler model fit. These simulated spectra using the simpler model are then fit with the more complex model. If thWhen applied correctly, in the regime of many counts per bin, a simple Gaussian-PDF χ^2 analysis will yield the exact same answers at a fraction of time investment and significantly less effort. Many of the analyses one would have to do using a Poisson statistical analysis could be done in the Gaussian regime. A goodness-of-fit is nearly immediately identifiable through χ^2_r, the reduced χ^2. The property that for

a fit parameter $\theta_{\mathbf{i}}$ near its best fit value $\bar{\theta}_{\mathbf{i}}$, the likelihood goes like

$$\exp(\frac{(\bar{\theta}_{\mathbf{i}} - \theta_{\mathbf{i}})^2}{\sigma_{\theta_i}^2} \tag{2.4}$$

makes calculating the uncertainty σ_{θ_i} trivial. In addition, the likelihood ratio test can be used to test for additional model components in Gaussian statistics as well, but it is often simplified to the simple F-test.e distribution of these fit statistics match the expectation value from the original fit to the spectrum using the more complex model (within 90% confidence), then the addition of the parameter is not statistically significant. However, if our expectation value falls well below this distribution, $<$ 5%, then the more complex model is favored. As an example (Figure 2.3), we have simulated the change in statistic when fitting to a spectrum simulated from the simpler parent model. This is plotted as the black distribution. We compare this distribution to the change in statistic when fitting the simpler and more complicated model to the spectrum extracted from the observed dataset. If the change in statistic is well within the simulated distribution, like in the case of the green example line, then we would favor the simpler model as better modeling the spectrum, and that the smaller statistic yielded by fitting to the more complicated model is coincidental. If, on the other hand, the change in statistic is larger than the simulated distribution, as in the red case, we would then favor the more complicated model as better modeling the spectrum.

Because the Cash statistic assumes a Poisson distribution, background subtraction cannot be used in order to analyze the source spectrum. Instead we model the background spectrum concurrently with the source spectrum. Because we are looking

at emission in the 0.3-8.0 keV band, we need to be able to correctly characterize the background of the ACIS chips in this energy band. We do this by extracting on-chip background regions. We then find a best fit to the extracted spectrum and use this additional model component in our analysis. For ACIS S-3 we find that the best fit model to the background consists of an absorbed CIE plasma and a powerlaw with a Gaussian component. The former models foreground diffuse emission while the latter models the particle background. For the ACIS S-2 and ACIS I-1 chips, we model the background as a powerlaw, with no other components needed to properly fit the background spectra. During spectral fitting to our regions we allow the background parameters of temperature, photon index, emission measure, Gaussian position, and Gaussian width to vary.

For a given parameter of the fit, we generate confidence intervals by calculating an analogue of the PDF near the statistical minimum directly. We vary it incrementally on a predetermined grid. For a given parameter grid point, we find the best fit. Using this technique, we can construct this pseudo-PDF for each fit parameter. We can then intuitively estimate the uncertainty in the fit parameter while taking into account correlation of parameters. Because these pdfs are not Gaussian (in some cases, very much so), it does not necessarily make sense to represent the confidence intervals in terms of the standard deviation σ. However, to avoid confusion, and for ease of comparison with other papers, we report the 67% confidence interval, analogous to the 1σ case. This is with the caveat that the intervals are almost never symmetric, and our limits do not behave like a confidence interval in the Gaussian

case. In particular, the 99.5% confidence interval is not usually a static multiplicative factor of the 67% confidence interval. An example is given in Figure 2.4.

Table 2.1. Churazov weighting vs. Cash statistic

Statistic	(kT-kT$_0$)/(kT$_0$)	(norm-norm$_0$)/(norm$_0$)	(Fe-Fe$_0$)/Fe$_0$	$(\tau - \tau_0)/\tau_0$
Churazov	(-0.072,+0.066)	(-0.070,+0.062)	(-0.118,+0.118)	(-0.083,+0.102)
Cash	(-0.028,+0.046)	(-0.051,+0.057)	(-0.097,+0.099)	(-0.062,+0.045)

Deviation of best fit parameters from the parent spectrum of Lee et al. (2011) Bar A region. The two values represent the upper and lower bounds of the 90 % error range.

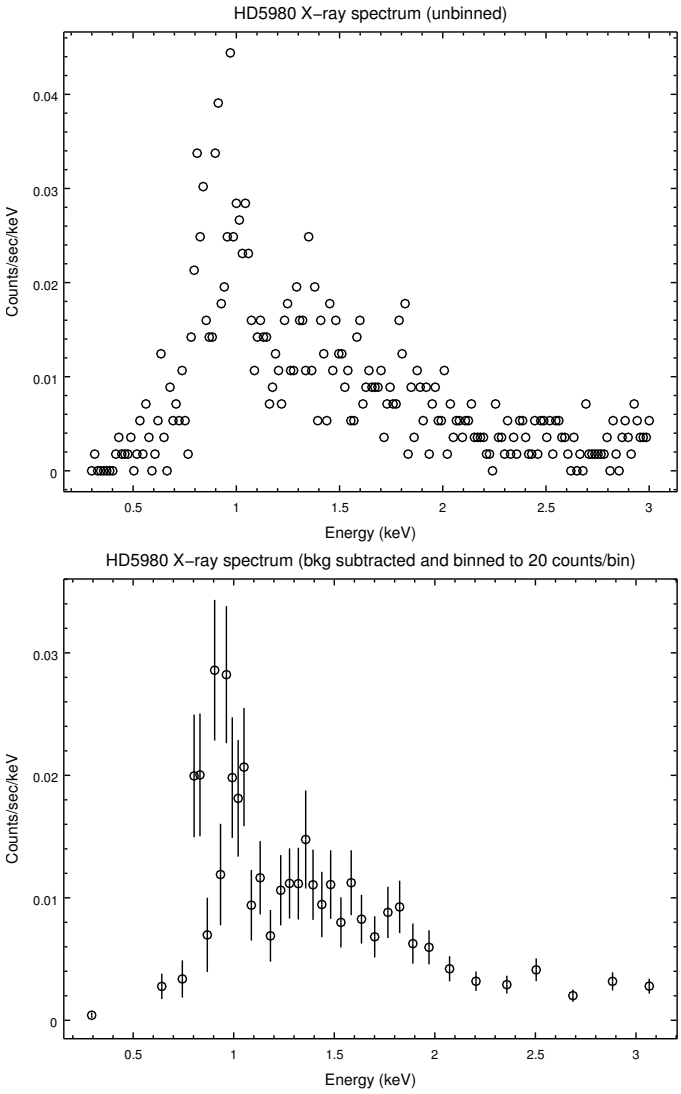

Figure 2.1. The X-ray spectrum of potential LBV HD 5980. The top is the HD 5980 spectrum unbinned, with Poisson errors. The bottom is the same spectrum, but background subtracted and binned to 20 counts per bin. The difference in effective spectral resolution between the top and bottom spectra is a factor of ~ 5.

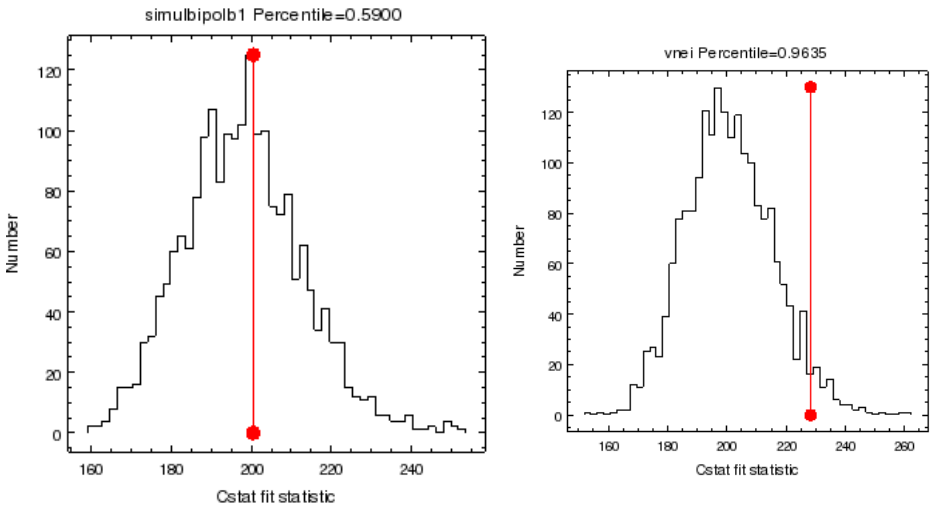

Figure 2.2. An example of using Monte Carlo simulations to analyze goodness-of-fit. In both the above figures, we have a simulated distribution of cstat statistics (black) expected, given the simulated parent model of a CIE plasma. The red line is the statistic yielded when the same model is fit to the "real" spectrum. The left is an example of a "good" fit, as the cstat obtained by fitting the real spectrum is within the expected distribution of simulated cstats. The right is an example of a "poor" fit (i.e. one that can be ruled out) because it is outside the expected distribution of cstats.

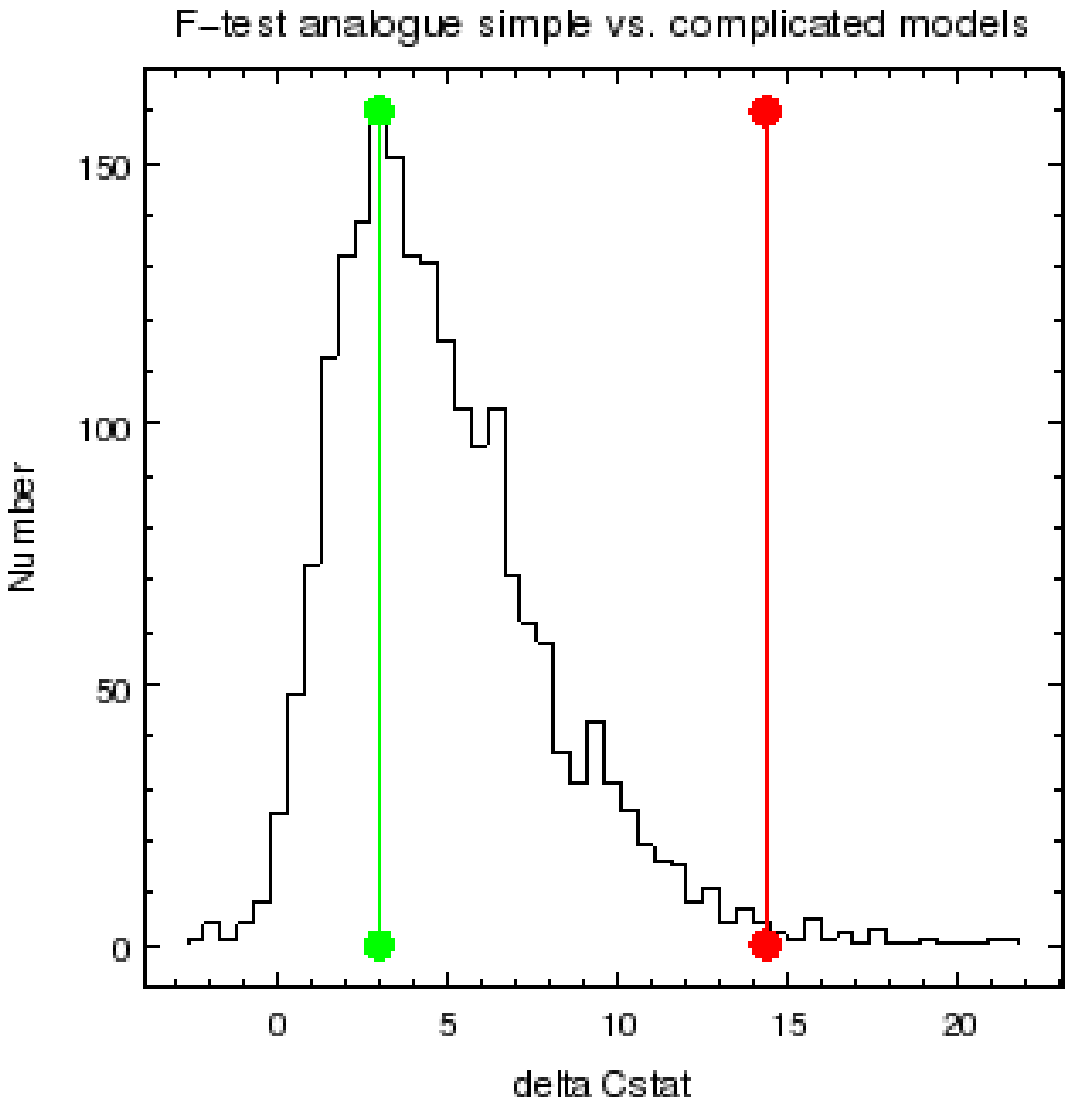

Figure 2.3. An example of using Monte Carlo simulations to compare two models, with the simpler model nested in the more complicated model. In this example, the X-axis is the difference in statistic between the two models, cstat_{simple}-$\text{cstat}_{complicated}$, and the y-axis is number of simulated fits. The simulated spectrum is of the simpler model, and the green and red curves represent the change in statistic of the "real" spectrum– in the green case, the simpler model would be favored, and the red case the more complicated model would be favored.

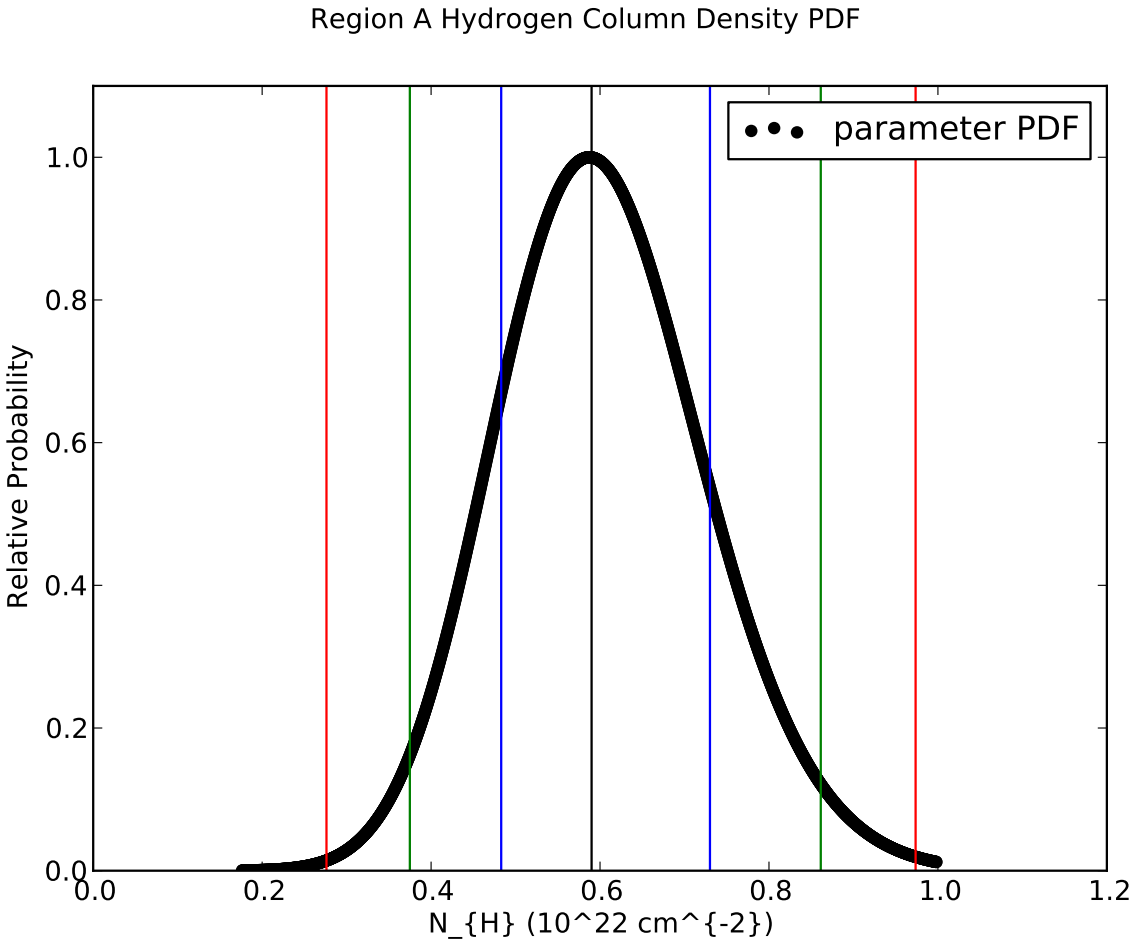

Figure 2.4. An example of direct pseudo-PDF construction using the fit statistic. The black dots are the "worst-case scenario PDF" of the parameter (in this example, the absorbing column density) versus its value in the fits. The vertical lines indicate the best fit parameter (black), as well as the analogue of 1-sigma (blue), 2-sigma (green) and 3-sigma (red) confidence intervals.

CHAPTER 3

POISSON STATISTICS APPLIED TO SUPERNOVA REMNANTS IN THE LOW COUNTS REGIME

Although much work has been produced in the *Chandra* and *XMM-Newton* era on the supernova remnant (SNR) population of the Small Magellanic Cloud (SMC), there are a subset of these remnants that are relatively understudied in the X-ray regime. This is at least in part due to their relative dimness in X-rays. van der Heyden et al. (2004) have performed a detailed study of 13 SNR using *XMM-Newton* and typed these objects based on morphology and spectral properties. In particular, they group three remnants, IKT 25, DEM S 128, and IKT 5 as probable Type Ia candidates. Their spectra are dominated by a single broad peak around 1 keV with little else in the way of line emission. This broad peak could be associated with Fe-L shell emission arising from shock heated ejecta thus leading to the Type Ia designations. In addition, they are markedly different from other SMC SNR in morphology, being very asymmetric in the soft X-ray band, as opposed to other, more symmetric core-collapse (CC) SNR. SNR 0102-72.3 is a well studied CC remnant (Flanagan et al. 2004) yet is highly symmetric both circularly and bilaterally. Other CC remnants in van der Heyden et al. (2004) also show high degrees of symmetry, such as IKT 6 (SNR 0049-73.6) and IKT 23 (SNR 0103-72.6).

The observations we present of IKT 25 total 112 ks over 2 observations of on-axis time on the ACIS S-3 chip (observation IDs 9100 and 9810). In these same observations, another of these remnants, DEM S 128, was serendipitously detected

on the ACIS S-2 chip ($\sim$ 6.5' off-axis). Due to its front illuminated nature, ACIS S-2 is less sensitive to the soft X-rays that dominate the emission of all three of these remnants. IKT 5 was also serendipitously observed as part of a deep field observation searching for X-ray binaries in the SMC. As such, IKT 5 appears off-axis ($\sim$ 7.5') for a total of 98 ks over 3 observations on the ACIS I-1 chip (observation IDs 7156, 8179 and 8481), which is also front illuminated.

In order to analyze and extract images and spectra from these observations, we use the Chandra Interactive Analysis of Observations (*CIAO*) software package (Fruscione et al. 2006) version 4.4 with the Calibration Database (CALDB) version 4.4.8. All the datasets are reprocessed using the *CIAO* script *chandra_repro* in order to ensure the most modern and relevant calibrations were applied to the datasets. The observations of each remnant are merged using the *dmmerge* tool. The X-ray images were binned to the natural Chandra ACIS instrument resolution. The X-ray data were adaptively smoothed using the CIAO tool *dmimgadapt* using a Gaussian kernel. The X-ray images, adaptively smoothed, can be seen at the top of Figures 3.1, 3.2, and 3.3.

To augment our analysis of these X-ray data, we examine the three remnants at different wavelengths. We analyze 20 cm data from the Australia Telescope Compact Array (ATCA), which were reduced using MIRIAD (Sault et al. 1995). The infrared and optical data we present were taken with the *Spitzer Space Telescope's* IRAC instrument, obtained through the *Spitzer* Heritage Archive, and optical data from the Magellanic Cloud Emission Line Survey (MCELS) in continuum subtracted Hα,

[S 2], and [O 3] bands. These particular wavebands have been included in order to qualitatively characterize the environments in which these SNR are located.

3.1 IKT 25

IKT 25 is the brightest of these three remnants in the X-ray band. Hughes & Smith (1994) presented ROSAT observations alongside CTIO Hα images and concluded that an unresolved point source in the X-ray has an Hα counterpart, thus suggesting a Be X-ray star association within the remnant. Lee et al. (2011) have performed a recent study utilizing the high spatial resolution of *Chandra* and find that this putative Be star is actually an extended knot of plasma. They find evidence of non-equilibrium plasma conditions and a marginal detection of Fe overabundance. Because it is seated within a complex environment, they conclude that IKT 25 is an example of a "prompt" Type Ia, whose progenitor system evolves to the supernova stage faster than typical (Borkowski et al. 2006).

For IKT 25, the best fit models and their best fit parameters are shown in Table 3.1. The spectra we obtained, with best-fit model overlayed, can be seen in Figure 3.4 and 3.5. Regions A, B, and D are best fit with a CIE plasma model with temperature of $\sim$ 1.0 keV. Region C is best fit with a two temperature model with a CIE component at kT $\sim$ 0.6 keV and an NEI component at kT $\sim$ 1.0 keV. When we fit this region with a one-temperature CIE plasma model, it resulted in a temperature of around 1.0 keV, similar to the other three regions. Adding the NEI component decreased our statistic from 202/195 to 188/192, which was significant (see Appendix A for further discussion). In all regions we require an enhanced Fe abundance in

order to fit the spectra, and in all regions the significance of the Fe overabundance was $> 5\sigma$. With the Wisp, we found the best fit model to be a two temperature model as in Region C, with one important difference: we found 5 σ enhanced silicon abundance in addition to enhanced iron abundance. The absorbing column density N_H varies greatly across the remnant, with Regions A, B, and D having a relatively small absorbing column density, at $<6 \times 10^{21} cm^{-5}$. Regions C and the Wisp have a much larger absorbing column density at $\sim 1.5 \times 10^{22} cm^{-5}$.

In comparison to van der Heyden et al. (2004), we find that the temperatures across the remnant are somewhat hotter, $\sim$ 1.0 keV compared to VDH04's finding 0.6 keV. They do not examine the spatial dependence of the absorption column density, and find a global absorbing column density of 4.1×10^{21} cm^{-2}, which, while consistent with our Regions A, B and D, we find to be very low compared to our Region C and Wisp fits, whose absorbing column density is as high as 1.5×10^{22} cm^{-2}. Unlike VDH04, we do not find any evidence for enhanced Ne in the remnant. This is likely a consequence of the models in this paper being more advanced than those used in VDH04. In particular the modeling of Fe L shell ions from 0.8-1.0 keV has improved immensely in APED. The additional lines significantly increase the total line flux contribution from species in this energy range, thus decreasing the importance of the Ne lines in comparison to the newly added suite of Fe lines. When comparing to Lee et al. (2011), we find a cooler temperature than their 2.0 keV. Lee et al. (2011) also do not examine the spatial variation in absorbing column density. Instead, they hold the column density across the remnant fixed the value of their global fit, 9.1×10^{21}

cm^{-2}. In Regions B and D, we find the absorbing column density to be as low as $\sim 3 \times 10^{21}$ cm^{-2}, with higher absorbing column density $\sim 1.5 \times 10^{22}$ cm^{-2} in Region C and the Wisp. In addition, our Fe overabundance is found to be more significant. Our norm-averaged Fe abundance across Regions A-D is 1.0 ± 0.1 which is 8 σ significance overabundant, whereas their norm-averaged Fe abundance across analogous regions Bar01-Bar04 is $\sim$ 1.08 $\pm$ 0.32, only 2.75 σ significance overabundant. It should be noted that a direct abundance comparison to Lee is difficult because they use the wrong abundances for the SMC. In particular, the abundances quoted in Table 1 of Lee et al. (2011) actually match the Table 1 column 8 values of Russell & Dopita (1992) which are the errors in the SMC abundances, not the abundances themselves therefore rendering the results suspect. Using the improved statistical approach with accurate abundances and up to date line lists, we have more tightly constrained physical parameters and detected a more robust Fe enhancement for IKT 25 in comparison to previous studies.

Our X-ray results indicate that, with the exception of enhanced Fe, our remnant is ISM dominated. We frame our X-ray results with data from other wavelengths to qualitatively probe how this remnant interacts with its environment. We use our IR and optical data (Figure 3.8) as images to compare with our X-ray and radio data for further insight into the emission of these remnants. From the radio contours of IKT 25 (Figure 3.8 a), we see evidence of a SN blast wave traveling through material that is roughly anticoincident with the X-ray emission of the remnant. The radio emission is highly coincident with the IR emission in the northeast. Synchrotron

emission in the lowest density regions of the shock may explain the radio emission while shock heated material with subsequent cooling emission explains the IR, optical, and X-ray emission, albeit at different densities. The optical emission shows primarily cooling lines from regions in the shell with densities somewhat higher than those in the X-ray plasma, whereas the 8 μm IR is dominated by PAH and dust emission. The IR emission is roughly anticoincident with Regions A, B, and D, and coincident with the Wisp region. The presence of significant IR emission suggests the existence of a local molecular cloud, which would give rise to the much higher line-of-sight absorption column density in the Wisp region. The lack of a high electron density derived from the X-ray fit suggests that the molecular cloud and the X-ray plasma are in physically distinct, non-interacting regions. The Wisp is also the only region in any of our remnants with enhanced Si, which is found to be $> 5\sigma$. This enhancement is quite evident in the Wisp spectrum as the large bump at 1.8 keV Si 13, especially when compared to all other spectra. This strongly suggests an enhancement of Si ejecta in this region. Its existence in the Wisp and absence in the rest of the remnant may imply that the local ISM in the Wisp region is less dense than in the other regions, which is corroborated by our low calculated densities from the X-ray spectral fits (Table 3.1). This suggests a cavity toward the east into which the supernova shock is propagating and possibly preserving the signs of both Fe and Si ejecta, thus supporting a Type Ia designation.

The bipolar morphology of IKT 25 may be due to asymmetry in the explosion mechanism of the progenitor system, or modification by the environment. In either

case, and especially for an asymmetric explosion, one might expect older plasma toward the center with more recently shocked gas in regions A and D. In this scenario we must be careful with the derived radii and velocities in regions B and C as they may be affected by line-of-sight projection. In other words, much of the emitting plasma in B or C may actually be at a large radius, comparable to regions A and D, yet just appear closer to the center in the X-ray data due to projection onto the plane of the sky. However, as seen from the X-ray spectral fit, there is a large column density associated with region C. Inspection of the optical data reveals a band of dense material stretching across region C, thus corresponding to the absorption seen in X-rays. In fact, the combination of X-ray, optical, IR, and radio data display a clear spherical geometry for this remnant. The band of material that is coincident in optical and radio wraps around the spherical remnant and is anti-coincident with the X-ray emission, except for that in region C. This suggests that this X-ray emission does not originate at large radii toward the observer, but must exist closer to the center of the remnant in this region. This constraint cannot be placed on region B. For this reason, we only compare ages from the internal region C with those found in A and D. For Regions A and D, we approximate the age using a Sedov solution, resulting in an age estimate of around 6000 years. The ionization parameter in Region C implies a shock timescale of longer than this, at around 20,000 years, depending on the assumed filling factor of the plasma. Therefore, the age structure of the remnant is consistent with a bipolar or directional flow of X-ray emitting material away from the center of the remnant and toward the locations of regions A and D. Given the

large amount of IR and optically detected material located in the band surrounding the X-ray emission, it is still difficult to determine if the X-ray emitting plasma is following a bipolar morphology due to a preferred explosion direction or pressure confinement from material in the environment.

Lee et al. (2011) have suggested that IKT 25 is produced by a so-called "prompt" Type Ia explosion mechanism. Our analysis supports this idea. Indeed, IKT 25 shares a great deal with the first two SNRs to be classified in this way, DEM L238 and DEM L249 (Borkowski et al. 2006). As in the Borkowski et al. remnants, the ionization parameter is large when compared to its Sedov age, and there is no obvious X-ray shell present. If we combine the results from all five regions of IKT 25, specifically the Fe abundance, the probability that they are consistent with or less than SMC abundance of 0.2 solar is vanishingly small, at $\sim 8 \times 10^{-24}$, which is equivalent to a $\sim 10\ \sigma$ significance. The global norm-averaged overabundance of greater than $8\ \sigma$ of Fe for IKT 25, and the presence of enhanced Si in the Wisp also argues strongly for the Type Ia designation.

3.2 DEM S 128

DEM S 128 was initially identified through a survey of Hα emission nebulae (Davies et al. 1976). Inoue et al. (1983) reported the first X-ray observation of this remnant and detected an extended X-ray counterpart nearby to this Hα region, naming it IKT 24. Filipović et al. (2000) reported a continuum 843 MHz Australian Telescope Compact Array (ATCA) observation of this remnant, and found significant radio emission. They compute radio spectral indices for sources coincident with

the remnant and nearby X-ray sources RX J0105.5-7213, RX J0105.6-7211, and RX J0104.9-7210. They classify RX 0105.5-7213 as a background active galactic nucleus, but are unable to classify the other two sources. They calculate a radio spectral index for DEM S 128 of α =-0.65 suggesting an evolved supernova remnant shock. Following this work, Filipović et al. (2005) observe the northern section of the remnant at 2.37 GHz and show that the emission is constrained to a few bright spots that are uncorrelated with previous X-ray data suggesting a complicated environment. Finally, Payne et al. (2007) report an S 2/Hα ratio of DEM S 128 of 0.6, which is also consistent with the shell of an evolved remnant.

The best fit model of the X-ray spectrum of DEM S 128 is given in Table 3.2, and is overlayed onto the extracted spectrum in Figure 3.6. With only one region extracted from DEM S 128, it is impossible to say anything about the spatial distribution of material in the SNR. However, in comparison to IKT 25, the absorbing column density is consistent with the Regions A, B and D at $\sim 3.5\times\ ^{21}cm^{-2}$. Again, Fe was necessary to vary in the fit. As in IKT 25, the Fe abundance was enhanced at $\sim$ 1.0 solar, and was very significant at $\sim 7\sigma$. All other elements were set to SMC abundance. Only one CIE thermal component was required, but the temperature was somewhat cooler than in IKT 25, at 0.65 keV.

Aside from the absorbing column density, we find different physical parameters for DEM S 128 than those determined in VDH04. As with IKT 25, we find a significantly enhanced Fe abundance (7σ). All other elements are consistent with SMC ISM values which contradicts the overabundance of Mg and Si reported in VDH03. An

overabundance of these species should be seen as clear line signatures at 1.3 and 1.8 keV, respectively, which is not observed in the spectrum (Figure 3.6). Our enhanced Fe abundance and lack of Mg argue more strongly for a Type Ia designation.

As in the case of IKT 25, the X-ray spectrum of DEM S 128 suggests it is ISM dominated, aside from Fe. In order to form a qualitative understanding of the interaction of DEM S 128 with its surroundings, we turn to other wavelengths for additional information. When examining IR data for DEM S 128, we see that there is very little in the way of extended sources. We observe an absence of dense shell emission from the SN blast wave, in stark contrast to IKT 25. In fact, we see no IR emission that is obviously associated with this SNR whatsoever. This may suggest a highly rarefied medium, which is consistent with the low density derived from the X-ray emission and Type Ia designation.

However, there are a number of discrete radio sources that are coincident with X-ray emission. Our point source analysis of the X-ray image revealed 7 point source detections. These sources are diagrammed in the center panel of Figure 3.9 which also overlays the radio data as white contours. The positions of these objects are given in Table 3.4. Of the seven, two were previously identified in X-ray point source catalogues, 2XMM J010536.3-720948 and CXO J010509-721146. Most of these X-ray point sources have no coincident radio emission greater than 5 times the local background flux. Intriguingly, one X-ray point source, labelled Source 2, does exhibit strong coincident radio emission. This object is only slightly extended when compared to the beam size of this mid-resolution radio image. Unfortunately, there

are only a total of 69 X-ray source counts, which is not enough to spectrally analyze this point source to confirm its non-thermal nature. However, the off-axis nature of the X-ray observation leads to a large point spread function and questionable discreteness of these sources. Also, high resolution radio data over multiple frequencies would determine the spectral index, which should be flat to be consistent with a PWN. On-axis, longer duration *Chandra* observations combined with higher resolution radio data could confirm that this source is indeed a PWN, contradicting the Type Ia designation. Further complicating the classification of DEM S 128 is its close positional coincidence with the star-forming region (SFR) DEM S 124. If DEM S 128 is a member of this SFR it seems likely that it is a CC remnant. This association would also explain the rarefied medium as being due to strong stellar winds.

The optical emission in of DEM S 128 is presented at the bottom of Figure 3.9. There is an optical circular shell filled with emission, but the center of this shell is some 45 parsecs spatially separated to the north of the X-ray remnant with no overlap. This optical feature is closer to the position of the original source labeled DEM S 128 by Davies et al. (1976), but the X-ray remnant is more consistent with the position of the source reported by Inoue et al. (1983). An arc of optical emission appears to surround the X-rays suggesting that the hotter gas is contained within this feature, but the high level of field confusion evident in the optical may make this association purely coincidental.

If the radio and X-ray bright source is a PWN, it strongly indicates that DEM S 128 is of core-collapse origin, which is perplexing given its Fe overabundance.

However, Borkowski et al. (2006) note that the progenitor systems of prompt Type Ia remnants are not known, and concedes that in spite of Fe overabundance, it is possible for a prompt Type Ia system to be of core collapse origin. So, even if our Source 2 is a PWN, it doesn't rule out the possibility that DEM S 128 is a prompt Type Ia SNR, but rather would elucidate the progenitor of some prompt Type Ia SNRs.

3.3 IKT 5

There is a paucity of observations on IKT 5. The first X-ray detection of IKT 5 was part of a large SMC survey by the *Einstein Observatory* (Inoue et al. 1983). In the optical, Payne et al. (2007) utilized long slit spectroscopy to analyze IKT 5 along with other remnants in the SMC and found it to have a very high S 2 6716 Å/ 6731Å line ratio. They also present a combined Hα and 843 MHz continuum image. Laycock et al. (2010) searched for X-ray binaries (XRB) in the SMC in the neighborhood of this remnant. They report finding an X-ray point source in the interior, labeled CXOU J004824-731918, but they conclude that due to the lack of a bright optical counterpart, this point source is likely not an X-ray binary. This leaves the possibility of another type of compact object.

The extraction regions for IKT 5 were chosen because the X-ray morphology suggests confinement in the north and extension toward the south. The best fits of the X-ray spectra obtained from the Northern and Southern regions can be found in Figure 3.7 and Table 3.3. As in IKT 25 and DEM S 128, we find an Fe overabundance in both the Northern and Southern regions of the remnant. The Northern region has

a $\sim$ 6 σ significant overabudnace at 0.8 solar. The Southern region has a higher Fe abundance at twice solar, but whose overabundance is much lower significance, at only $\sim$ 2.5 σ. The Northern region is well fit by a 0.94 keV equilibrium plasma. The Southern region contains a lower temperature equilibrium plasma at 0.56 keV combined with a higher temperature nonequilibrium plasma at 0.98 keV.

The X-ray results in this remnant are perhaps the most perplexing of the three remnants. The Northern region has an Fe overabundance at 0.8 solar, which is significantly above SMC abundance by about 4 σ, whereas the Southern region has an Fe abundance of twice solar, but the error bars on this particular region are large enough to be consistent with SMC ISM. As in Region C and the Wisp of IKT 25, the Southern region's CIE fit is relatively cool at 0.56 keV, whereas the NEI component is at 1.0 keV. The values of the absorbing column density across IKT 5 found by VDH04 are consistent with our results. VDH04 find a very high ionization timescale, and while this is consistent with our Upper Region, which is in CIE, it is inconsistent with our fit result in the Lower Region, which has a component out of ionization equilibrium with a timescale that is smaller than the lower limit listed in VDH04. As with IKT 25, VDH04 find enhanced Ne that we do not require in order for a good fit. Again, this is mostly due to the overlap of the Fe-L shell and the Ne-K shell in energy. The X-ray results on their own, as with IKT 25 and DEM S 128, suggest a Type Ia origin.

To explore this classification further, we perform a point source analysis on IKT 5 given previous suggestions of a point source (Laycock et al. 2010; van der

Heyden et al. 2004). We detect a source within the remnant that is coincident with the CXOU J004824-731918 source reported in Laycock et al. (2010). Figure 3.10 (upper right) shows the 3σ *wavdetect* psf extent as a green ellipse with high energy, 2.0–8.0 keV emission in white contours. The peak of the high energy emission is coincident with the location of the point source suggesting that this source is not simply a bright knot of emission from the SNR. Given the Laycock et al. (2010) conclusion that the point source is likely not an XRB, the possibility exists that this source is a PWN or compact central object. Spectra extracted from just the point source region were too low significance to perform meaningful spectral fits to verify this possibility. Longer, on-axis Chandra observations are necessary in order to further constrain the nature of this point source, yet the current characteristics challenge a typical Type Ia designation.

As in the IKT 25 and DEM S 128 cases, only Fe was overabundant, indicating that this is a highly ISM-dominated remnant. Figure 3.10 (upper left) shows that to the southeast of the X-ray remnant there is a small, diffuse knot of infrared emission that is roughly anticoincident with the X-ray emission in the Southern region. We find from the shorter wavelength IR images (not presented here) that this knot is actually unresolved point source emission from a star cluster in the area, and is likely not associated with the remnant. Also evident is an IR source in the middle of the remnant, coincident with a known red supergiant 2MASS J00490818-7314155 (Massey & Olsen 2003). It is unclear to what extent any of the IR emission in this field is associated with IKT 5.

The radio observation for IKT 5 is also shown in the upper left panel of Figure 3.10. The hard X-ray point source found in our analysis is not detected in the radio, making a PWN within the remnant questionable. However, the telescope array was optimized for diffuse emission. An observation using an array configuration optimized for spatial resolution is necessary to determine the strength of the point source radio emission. In addition, further to the west of the remnant there is a half-shell in the radio consistent with shocked gas. This half-shell appears to have its center positionally consistent with the X-ray remnant. The optical emission completes this western radio shell in Hα and [S 2] (Figure 3.10, bottom left). The optical image also reveals a secondary, inner optical bubble that appears just exterior to the X-ray emission. The inner bubble of this "double bubble" structure could be the SN shock front. This volume would then be filled with hot, X-ray emitting gas. The outer, larger bubble is clearly also shocked gas, but is far outside the remnant. Such a shock could be due to the progenitor system. A massive star progenitor could have blown a cavity with its strong stellar wind. The ~ 50 pc physical size of this bubble is consistent with typical wind speeds (hundreds of km/sec) and lifetimes (10^5–10^6 years) of massive stars. The inner SN blast wave is in the process of catching up with the outer bubble, which has a head start on the order of the lifetime of the massive star.

Our analysis suggests that IKT 5 may not be of Type Ia origin. The detection of the possible X-ray point source with surrounding high energy emission is indicative of a leftover compact object, thus being consistent with the picture of a massive pro-

genitor, as are the combined optical and radio data. However, the large Fe abundance argues against at least a typical core collapse SNR. In addition, the current lack of coincident radio emission argues that the potential compact object is unlikely to be a PWN, yet higher resolution data are needed for verification. As with DEM S 128, the X-ray observation of IKT 5 was well off-axis thus leading to a poor PSF and questionable point source detection. Given the environmental conditions present in the multi-wavelength analysis there is stronger evidence of a core-collapse origin for IKT 5. However, we cannot rule out the possibilty that IKT 5 is another member of the same class of prompt Type Ia SNR as IKT 25 and DEM s 128. It is important to acquire higher quality, on-axis, longer exposure X-ray data to ensure the nature of this point source and its high energy emission, as well as high-resolution radio data. This would clarify the classification of this SNR and identify the central compact object.

3.4 IKT 18

IKT 18 is an SNR candidate adjacent to the star forming region NGC 346 first detected by the *Einstein X-ray Observatory* (Inoue et al. 1983). Ye & Turtle (1991) found a nonthermal radio source at this same position, labeling it SNR 005-7226. Along the line of sight of the putative remnant lies the point source HD 5980. HD 5980 is a system with two eclipsing emission line stars with a short 19.3 day orbit (Breysacher & Perrier 1980) and a third component O-type star. The two close-orbiting companions have been spectroscopically classified as Wolf-Rayet stars of type WN3 and WN4. A radial velocity study of optical N 4 and N 5 profiles place

mass estimates of these two stars with Star A estimated at 58-79 $M_{\odot}$ and Star B 51-67 $M_{\odot}$ (Foellmi et al. 2008). In 1993 and 1994, this system underwent a massive eruption, during which its V-magnitude decreased by 3. As the outburst occured, Star A underwent changes to its Wolf-Rayet spectral subtyping from WN3 to WN11 (Barba et al. 1996). This has led to HD 5980 being classified as a luminous blue variable (LBV) star.

X-ray data from the *Chandra X-ray Observatory* Advanced Camera for Imaging Spectroscopy (ACIS) were obtained in 2001 and are presented in Nazé et al. (2002). They report detecting variability of HD 5980 by a factor of two and spectroscopically detect the formation of an LBV nebula through a hot thermal X-ray plasma that is not resolvable in the image. Their spectral modeling suggests that this nebula is very hot, at around 7.0 keV. However, they concede that this X-ray emission could also be due to colliding winds between the close binary of Star A and Star B. They note that the source HD 5980 has a very low signal to noise ratio, and so their modelling was limited to simpler models. They do not attempt to detect whether the diffuse emission in IKT 18 had enhanced abundance of any metal, but come to the conclusion that IKT 18 is likely a SNR. In addition, they come to the conclusion that HD 5980 is in the background of IKT 18 due to higher column density of absorbing material when compared to the remnant.

If the source HD 5980 is indeed an LBV, we might expect significant variation in both X-ray spectrum and X-ray luminosity on the order of a decade, as has been seen in e.g. η Carinae (Corcoran et al. 2001), which reached an X-ray minimum in

2009 (Hamaguchi et al. 2014). Koenigsberger et al. (2010) report that prior to and during its 1994 eruption, HD 5980 exhibited a large UV emission line flux, and noted that it exhibited a similarly large UV emission line flux some 40 years earlier, even though no corresponding optical increase in flux was noted in the 1950 epoch. Using this, they proposed a tentative 40 year period of massive outbursting of the source HD 5980. However, continuous monitoring of HD 5980 has not occured, and there was not a corresponding outburst directly observed in 1950, so this period is somewhat suspect.

We present two separate datasets, one taken in 2001 and another taken in 2013. The 2001 epoch data is a 100 ksec observation in which IKT 18 and HD 5980 are imaged on the ACIS-I3 chip. The 2013 epoch data is 40 ksec in length, and IKT 18 and HD 5980 were imaged on the ACIS-S4 chip. In order to analyze and extract images and spectra from these observations, we use the Chandra Interactive Analysis of Observations (*CIAO*) software package (Fruscione et al. 2006) version 4.5 with the Calibration Database (CALDB) version 4.4.8. All the datasets are reprocessed using the *CIAO* script *chandra_repro* in order to ensure the most modern and relevant calibrations are applied to the datasets. The more recent 2013 epoch X-ray data are shown in Figure 3.11, binned by a factor of 4 pixels where the natural ACIS-S resolution is at 0.48“ per pixel, and smoothed over a Gaussian kernel of 0.96“. The 2001 epoch data were previously analyzed by Nazé et al. (2002). For consistency, rather than rely on their conclusions, we reprocess both datasets in the aforementioned way so that any systematic differences introduced by reprocessing the data could be

accounted for.

In order to better visualize the spatial and spectral contributions to the X-ray data, we separate the data into three bands, displayed in Figure 3.12. We choose a low-energy band from 0.3-0.8 keV band, which is dominated by oxygen lines. We pick a middle-energy band from 0.8-1.2 keV, which we expect to be dominated particularly by Ne 9 and Ne 10, which should be strong in the case of core-collapse remnants, as well as the Fe-L shell lines. Finally, our high energy band from 1.2-8.0 keV could be dominated either by nonthermal processes or continuum processes of very hot (kT $>$1 keV) gas and could also contain Mg, Si and S lines, which will dominate for cooler (kT $\lesssim$ 1 keV).

To augment our analysis of these X-ray data, we examine HD 5980 and IKT 18 in the 20 cm band. These radio data were obtained from the Australia Telescope Compact Array (ATCA), and reduced using MIRIAD (Sault et al. 1995). The radio contours are shown in Figure 3.12. These contours correspond to 3, 6 and 9 times the local background.

Extraction regions for spectral analysis of IKT 18 are determined through inspection of the X-ray images. The *CIAO* script *specextract* is used to extract spectra, as well as produce the response matrices. We perform a point source extraction to produce the extraction region for HD 5980, as well as to exclude its contribution to IKT 18. To do this, we used the *CIAO* tool *wavdetect* with wavelet transformation scales of 0.5", 1", 2", and 4". The output provides region files that encompass the 3σ extent of HD 5980 where σ is the uncertainty in the point spread function (PSF).

To utilize this tool, we produced the expected off-axis PSF of *Chandra* using the *mkpsfmap* CIAO tool. The resulting extraction regions are shown in Figure 3.13. The region labelled "IKT 18 Annulus" encompasses the diffuse emission from the SNR while the region labelled HD 5980 is the 3σ region determined by *wavdetect*.

The source spectral models are convolved through two separate absorption columns: one representing galactic absorption with absorbers at galactic abundances, *xstbabs*, and one representing absorption within the SMC with SMC abundances, *xstbvarabs*. The galactic component is frozen at $N_H = 0.075 \times 10^{22}$ cm^{-2} (Dickey & Lockman 1990), while the SMC component's hydrogen column density is allowed to vary. We choose *xstbabs*.

We model the on-chip X-ray background as a simple powerlaw. This choice is somewhat arbitrary, but it adequately fits the form of the spectrum extracted in both epochs. This suffices, as we are not concerned with the nature of the background emission, and are only modeling it to account for its contribution to the source spectra extracted from the IKT 18 Annulus and the HD 5980 source. We use this on-chip background in addition to a source model to fit the spectrum extracted from the IKT 18 annulus. The HD 5980 region is modeled as a source model representing HD 5980, added to the IKT 18 source model and the on-chip background. Because we expect the diffuse emission from the IKT 18 Annulus to contribute a noticeable amount of emission to the HD 5980 region, the background spectrum and those extracted from the IKT 18 Annulus and HD 5980 source are fit simultaneously. Thus the parameters are varied until the combined statistic is minimized for all three spectra. We perform

separate fits in this way for the 2001 epoch and the 2013 epoch.

3.4.1 IKT 18 Annulus

In both the 2001 and 2013 epochs, we find that the emission from the IKT 18 Annulus is consistent with an NEI plasma at 0.58 keV. This plasma is almost entirely not-absorbed within the SMC, as the best fit absorbing hydrogen column density is small, with an upper bound of 6.6×10^{20} cm^{-2}. The ionization parameter is $\sim 2 \times 10^{11}$ s cm^{-3} in the 2001 epoch, and $\sim 1.2 \times 10^{12}$ s cm^{-3} in the 2013 epoch. However, their errors are such that both fits are consistent with an ionization parameter of $\sim 3.2 \times 10^{11}$ s cm^{-3}. Within the annulus, Ne is found to be overabundant in comparison to typical SMC ISM values of 0.2 solar (Russell & Dopita 1992). In the 2001 epoch, this overabundance is $\sim 3.6\ \sigma$ significant, whereas in the 2013 epoch, this overabundance is $\sim 2.6\ \sigma$ significant. This combines to yield an overabundance that is $4.4\ \sigma$ significant.

Using the parameters of our spectral fits we can calculate additional characteristics such as plasma density and shock velocity. Solving the Rankine-Hugoniot relations in the strong shock case with $\gamma = 5/3$ gives the post-shock temperature as a function of shock velocity, $kT = (3/16)\mu m_p v^2$, with the average mass per particle $\mu = 0.6$. We assume that $T_e \sim T_{ion}$ as expected through Coulomb collisions in a plasma with a temperature of $\sim 10^6$ K and $n_e \sim 1$ cm^{-3} (Draine 2011). If the electrons and ions are not in temperature equilibrium then the calculated velocities signify lower bounds. We can also estimate the age of the remnant from the equilibrium shock velocities. Assuming that each remnant can be described by a Sedov solution (Spitzer 1998), the time since shock heating can be calculated as $t = (2/5)R/v$, where R is

the estimated shock distance from the center. The density is found using the *norm* parameter for each component, where $norm = [10^{-14}/(4\pi D^2)] \int n_e n_H dV$ where D is the distance to the source, in this case the SMC. The value $\int n_e n_H dV$ is the emission measure, where n_e and n_H are the electron and proton densities, and V is the volume of emitting plasma. A value of 61.3 kpc is used for D (Hilditch et al. 2005) and we assume that $n_e = 1.2 n_H$. We include a filling factor, f, which ranges from 0 to 1, to account for the fraction of the volume actually filled with X-ray emitting plasma. Given the ambient density, the temperature, and the radius of the remnant, we can estimate the initial input energy as $E_{51} = r_5^3 n_e (kT)$ where E_{51} is the input energy in units of 10^{51} ergs, r_5 is the radius in units of 5 pc, n_e is the density in units of cm^{-3}, and kT is the temperature in units of keV.

The temperature of the diffuse plasma is consistent with a shock velocity of 700 km/s. With an approximate radius of $\sim$ 22 pc, this yields a derived age of 12,400 yrs. Assuming an annular spheroid with an inner radius equal to the average radius of the HD5980 extraction region, and an outer radius which is the average radius of the IKT 18 Annulus, the norm from our spectral fits yield the approximate ambient density is 0.15 cm$^{-3}/f^{1/2}$, where f is the geometric filling factor. This, when combined with the ionization parameter, yields a shock timescale of 8400 yrs $f^{1/2}$, and an input energy of $1.7 \times 10^{51}/f^{1/2}$ ergs. However, the SNR is in the vicinity of NGC 346. The medium into which the SNR is expanding may be far from isotropic, so a Sedov-like explosion model may be inappropriate. An increase in the ambient density will accelerate the evolution of the SNR. This means that the Sedov-derived

age of 12,400 years is an upper bound, and the age of 8,400 years of the ionization parameter is a lower bound to the actual age of the remnant.

The large input energy derived from our spectral fits confirm that IKT 18 is the product of a SN explosion as opposed to a very old, very large LBV. The diffuse emission around IKT 18 is highly suggestive of a SNR that is ISM-dominated. The significant overabundance of Ne and no such indication of Fe overabundance argues for a CC-type designation. CC-type remnants are more likely to be in the proximity of a SFR, so IKT 18 being positionally very near the NGC 346 SFR is also consistent with this interpretation as well. The estimated age of this SNR of $\sim$ 10000 yrs also argues against IKT 18 corresponding to an LBV nebula. The expected lifetime of an LBV is $\sim$ 20,000 yrs (Humphreys 1991). Assuming that any previous outbursts of the system were ejected at about the same velocity as the 1994 outburst, $\sim$ 400 km/s (Koenigsberger et al. 2000), this would require a travel-time of $\gtrsim$ 50000 yrs. Thus we rule out IKT 18 itself as being an LBV nebula. This result provides evidence against an association between IKT 18 and HD 5980.

The radio emission in the vicinity of IKT 18 is coincident with the X-ray emission and indicative of SNR radio morphology as seen in Figure 3.12. We label two seperate components to the radio emission– an X-ray loud component, consistent with our IKT 18 Annulus, and an X-ray quiet component, which we label NGC 346. The radio component coincident with the IKT 18 Annulus is almost certainly part of the non-thermal X-ray source reported by Ye & Turtle (1991), further confirming its SNR nature. However, while the presence of 20 cm radio emission is consistent with

a SN blast wave, there is not a clear circular shell at other wavelengths corresponding to this blast wave. The radio emission does not get brighter towards the center of the remnant, as you might expect if the remnant were plerionic. The X-ray quiet component of the radio emission likely comes from the SFR NGC 346. It is possible that the progenitor of the IKT 18 SNR was a member of NGC 346, but these are likely physically distinct radio sources.

3.4.2 HD 5980

In the 2001 epoch, we find that the HD 5980 region is best fit by an NEI thermal model. The temperature derived from this model is very hot, with a lower bound of 4 keV. The absorbing column density is 1.5×10^{21} cm^{-2}, but is consistent with zero absorption given the error bars. The ionization parameter is small compared to the diffuse emission at $\sim 2 \times 10^{10}$ s cm^{-3}. Our best fit for a non-thermal source model in this epoch is significantly statistically worse at cash/dof of $\sim$ 867/675.

In the 2013 epoch, we find that HD 5980 is better fit by an absorbed powerlaw. The upper bound of the absorbing column density is 2×10^{21} cm^{-2}. The photon index of the best fit model is 1.9, and the flux at 1 keV is $\sim 6 \times 10^{-5}$ photons keV^{-1} cm $^{-2}$ s^{-1}. When we fit a thermal model source spectrum, the best fit is *xsvphabs* $\times$ *vnei*, which fits comparably well statistically speaking (a cash/dof of 821/675), but the parameters of the best fit indicate a low ionization parameter of $\lesssim 2 \times 10^{8}$ s cm^{-3}. In addition, our *bbody* fit to the 2013 epoch spectrum was significantly worse (cash/dof of 2200/678), and our best fit *bknpower* was degenerate with our *powerlaw* fit. Our best fit *srcut* fit yielded a best fit comparable to the *powerlaw* fit (cash/dof of

813/677), with a radio spectral index of 0.61, a norm of 8.3×10^{-3} Jy, and a breaking frequency of 4.2×10^{9} GHz, but since there was no obvious radio emission from the source in the 20 cm band, we disregard this fit.

In the 2001 epoch, the temperature of >3.9 keV is entirely consistent with the temperature obtained by Nazé et al. (2002). If we consider the best fit thermal model, this lower bound is consistent with estimates of the fast wind phase observed in post-outburst UV emission lines of $\sim$ 1600 km/s (Georgiev et al. 2011), corresponding to a temperature of $\sim$ 8 keV. However, the hot thermal plasma modeled in the 2001 epoch has changed significantly in the 2013 epoch. Our model for the 2001 epoch has an absorbed X-ray luminosity of 1.7×10^{34} ergs/second in the 0.3-10.0 keV band. This corresponds to an unabsorbed X-ray flux of 2×10^{34} ergs/second, which is consistent with the X-ray luminosity over the same band of Nazé et al. (2002). In the 2013 epoch we find that HD 5980 exhibits an absorbed X-ray luminosity L_X of 1.2×10^{35} ergs/s in the 0.3-10.0 keV band, independent of a preferred best fit between statistically redundant thermal and powerlaw fits. This is an order of magnitude higher than the unabsorbed X-ray flux in the same energy band in the 2001 epoch Nazé et al. (2002) and, indeed is comparable to estimates of the X-ray flux of η Carinae (Ishibashi et al. 1999).

In addition, the dominant X-ray emission has transitioned from being line-dominated in the 2001 epoch to continuum dominated in the 2013 epoch. The decreased ionization parameter indicates that the plasma of the 2013 epoch is not the same as the plasma of the 2001 epoch, despite their similar temperatures. The ratio

of the thermal norm parameters from the 2013 epoch and the 2001 epoch yields that the density of the plasma has increased by a factor of ~ 4. This means that the X-ray emission from HD 5980 is not simply an evolution of the same plasma from the 2001 epoch. This could be due to some impulsive heating process that has taken place in the system. However, it could also be due to an increase in wind-wind emission due to orbital motions of the system. If the 2013 epoch observation were taken closer to periastron that the 2001 epoch observation, we would expect more nascent wind-wind interaction, leading to a higher density, underionized plasma, as the ionization has yet to equilibrate given the shorter timescale since the creation of this plasma. This interpretation is consistent with a smaller ionization parameter in the 2013 epoch, as reflected by the thermal fit.

If instead we favor the powerlaw fit, the change of the X-ray luminosity could be interpreted as an increase in the non-thermal population of electrons. Leyder et al. (2010) study the X-ray emission from η Carinae wherein they utilize both thermal and non-thermal components to model the spectrum. They interpret the change in observed X-ray flux as an increase in particle acceleration in the wind-wind interaction zone. The powerlaw associated with their model has a photon index of 1.8 ± 0.4, which is consistent with our powerlaw fit. If HD 5980 is closer to periastron in the 2013 epoch, it is reasonable to suspect that there will be an increase in the non-thermal electron population produced in the wind-wind interaction region, similar to η Carinae. This may lead to a non-thermal emission mechanism producing the powerlaw we see in the 2013 epoch dominating the previously observed thermal

spectrum in the 2001 epoch.

Table 3.1. Best Fit Parameters for IKT 25 by extraction region.

Region	Best Fit Model	cstat/dof	1-(P-value)	$N_{H,SMC}$ ($10^{22} cm^{-2}$)	kT_{vapec} (keV)	A_{Fe}	$norm_{vapec}$ ($10^{-5} A^a$)	kT_{nei} (keV)	τ_{nei} ($10^{11} cm^{-3} s$)	$norm_{nei}$ ($10^{-5} A$)	A_{Si}
A	$tbabs_{gal} \times tbvarabs_{SMC} \times vapec$	202/195	75.0 %	$0.58^{+0.29}_{-0.30}$	$0.95^{+0.03}_{-0.03}$	$1.2^{+0.2}_{-0.2}$	$6.1^{+0.7}_{-0.7}$				
B	$tbabs_{gal} \times tbvarabs_{SMC} \times vapec$	204/195	24.4 %	$0.32^{+0.31}_{-0.21}$	$0.92^{+0.05}_{-0.09}$	$0.8^{+0.2}_{-0.1}$	$6.2^{+0.5}_{-1.0}$				
C	$tbabs_{gal} \times tbvarabs_{SMC} \times (vapec + vnei)$	188/192	10.6 %	$1.4^{+0.6}_{-0.4}$	$0.68^{+0.04}_{-0.04}$	$0.7^{+0.2}_{-0.1}$	$1.2^{+0.2}_{-0.2}$	$0.98^{+0.05}_{-0.05}$	$2.8^{+0.2}_{-0.2}$	$1.4^{+0.2}_{-0.8}$	
D	$tbabs_{gal} \times tbvarabs_{SMC} \times vapec$	189/195	86.8 %	$0.27^{+0.19}_{-0.18}$	$1.03^{+0.03}_{-0.03}$	$0.8^{+0.1}_{-0.1}$	$8.9^{+0.4}_{-0.7}$				
Wisp	$tbabs_{gal} \times tbvarabs_{SMC} \times (vapec + vnei)$	219/191	89.0 %	$1.3^{+1.3}_{-0.3}$	$0.58^{+0.04}_{-0.04}$	$0.7^{+0.2}_{-0.1}$	$1.7^{+0.5}_{-0.4}$	$0.9^{+0.2}_{-0.1}$	>2.0	$0.9^{+0.4}_{-0.4}$	$1.3^{+0.3}_{-0.2}$

Spectral fitting results by region listed in Figure 3.1. The remnant and regions are listed in the first two columns, with the next column indicating the best fit model.

Note.—Errors shown are analogous to 1σ. Abundances are shown relative to solar with solar values equal to 1.

[a]Normalization parameter, where $A = [10^{-14}/(4\pi D^2)] \int n_e n_H dV$, D is the distance to the SMC and the integral is the emission measure.

Table 3.2. Best Fit Parameters for DEM S 128.

Best Fit Model	cstat/dof	1-(p-value)	$N_{H,SMC}$ ($10^{22} cm^{-2}$)	kT_{vapec} (keV)	A_{Fe}	$norm_{vapec}$ ($10^{-5} A^a$)
tbabs$_{gal}$ × tbvarabs$_{SMC}$ × vapec	219/200	12.4 %	$0.35^{+0.14}_{-0.12}$	$0.65^{+0.03}_{-0.03}$	$0.9^{+0.2}_{-0.1}$	15^{+3}_{-2}

Spectral fitting results of DEM S 128 with extraction and background regions and Figure 3.2. The remnant and regions are listed in the first two columns, with the next column indicating the best fit model.

Note.—Errors shown are 1σ. Abundances are shown relative to solar with solar values equal to 1.

[a]Normalization parameter, where $A = [10^{-14}/(4\pi D^2)] \int n_e n_H dV$, D is the distance to the SMC and the integral is the emission measure.

Table 3.3. Best Fit Parameters for IKT 5 by extraction region.

Region	Best Fit Model	cstat/dof	1-(p-value)	$N_{H,SMC}$ ($10^{22} cm^{-2}$)	kT_{vapec} (keV)	A_{Fe}	$norm_{vapec}$ ($10^{-5} A^a$)	kT_{nei} (keV)	τ_{nei} ($10^{11} cm^{-3} s$)	$norm_{nei}$
Northern	$\text{tbabs}_{gal} \times \text{tbvarabs}_{SMC} \times \text{vapec}$	227/197	77.5 %	$0.3^{+0.1}_{-0.1}$	$0.94^{+0.03}_{-0.03}$	$0.8^{+0.2}_{-0.1}$	$6.3^{+0.6}_{-0.6}$			
Southern	$\text{tbabs}_{gal} \times \text{tbvarabs}_{SMC} \times (\text{vapec} + \text{vnei})$	221/194	79.1 %	$0.23^{+0.08}_{-0.08}$	$0.56^{+0.03}_{-0.03}$	$2.0^{+1.3}_{-0.7}$	$0.6^{+0.8}_{-0.8}$	$1.0^{+0.1}_{-0.1}$	$1.7^{0.8}_{-0.3}$	$1.8^{1.0}_{0.2}$

Spectral fitting results by region listed in Figure 3.3. The remnant and regions are listed in the first two columns, with the next column indicating the best fit model.

Note.—Errors shown are 1σ. Abundances are shown relative to solar with solar values equal to 1.

[a]Normalization parameter, where $A = [10^{-14}/(4\pi D^2)] \int n_e n_H dV$, D is the distance to the SMC and the integral is the emission measure.

Table 3.4. List of point sources in DEM S 128

J2000 coordinates		Previously reported name (if applicable)	Radio Coincident?
Right Ascension	Declination		
01 : 05 : 36.3	-72°9' 48.9"	2XMM J010536.3 -720948	No
01 : 05 : 30.9	-72°10' 21.5"		Yes
01 : 05 : 24.9	-72°11' 16.1"		Possible
01 : 05 : 9.7	-72°11' 48.0"	CXO J010509 -721146	No
01 : 04 : 59.9	-72°11' 47.7"		No
01 : 05 : 50.5	-72°12' 37.1"		
01 : 05 : 33.0	-72°13' 31.5"		

A list of the point sources within and around the supernova remnant DEM S 128. The point sources were detected using the *CIAO* tool *wavdetect*. Previously discovered point sources with names are given in the rightmost column.

Table 3.5. Physical parameters of the SNR.

Remnant	Region	$v_{shock,cie}$ km/s	radius pc	Sedov age yr	$n_{e,cie}$ $cm^{-3}/f^{1/2}$	t_{shock} yr × $f^{1/2}$	$v_{shock,nei}$ km/s	$n_{e,nei}$ $cm^{-3}/f^{1/2}$
IKT 25	Region A	899	14.5	6300	0.25			
	Region B	885			0.45			
	Region C	761			0.15	20000	913	0.17
	Region D	936	14.3	6000	0.25			
	Wisp	703			0.08		875	0.06
DEM S 128		755	21.9	11000	0.08			
IKT 5	Upper	894	13.9	6100	0.10			
	Lower	691	14.1		0.05	38000	923	0.08

Physical parameters derived from the fit parameters in Tables 3.1, 3.2 and 3.3.
Shock velocity was calculated using the temperature from Tables 3.1, 3.2 and 3.3.

Table 3.6. Best Fit Parameters for IKT 18 and HD 5980.

IKT 18 Annulus							
Epoch	Best fit model	cash/dof	Best fit parameters				
2001	xsvnei	835/675	nH (10^{20}cm^{-2})	kT (keV)	Ne (solar)	log(Tau/s cm−3)	norm ($10^{-5}A^1$)
			<4.0	$0.58^{0.01}_{0.01}$	$0.31^{0.03}_{0.03}$	$11.3^{0.1}_{0.1}$	49^{15}_{10}
2013	xsvnei	811/678	nH (10^{20}cm^{-2})	kT (keV)	Ne (solar)	log(Tau/s cm−3)	norm ($10^{-5}A^1$)
			<6.6	$0.58^{0.02}_{0.02}$	$0.43^{0.08}_{0.05}$	$12.1^{0.1}_{0.3}$	92^{10}_{6}
HD 5980							
Epoch	Best fit model	cash/dof	Best fit parameters				
2001	xsvnei	835/675	nH (10^{20}cm^{-2})	kT (keV)	Ne (solar)	log(Tau/s cm−3)	norm ($10^{-5}A^1$)
			$15^{0.03}_{0.10}$	>3.9	0.31[2]	$10.4^{0.4}_{0.6}$	$1.6^{0.2}_{2.7}$
2013	xspowerlaw	811/678	nH (10^{20}cm^{-2})	Photon index (unitless)		norm (photons keV^{-1} cm^{-2} s^{-1})	
			<20	$1.9^{0.1}_{0.2}$		$6.3^{0.3}_{0.7} \times 10^{-5}$	
2013	xsvnei	821/675	nH (10^{20}cm^{-2})	kT (keV)	Ne (solar)	log(Tau/s cm−3)	norm ($10^{-5}A^1$)
			<0.05	$4.0\ ^{0.6}_{0.7}$	0.43[2]	<8.3	$24^{0.1}_{7.9}$

Spectral fitting results by region listed in Figure 3.13. The remnant and regions are listed in the first two columns, with the next column indicating the best fit model. The absorbing column density listed is from the model *tbvarabs* at SMC abundances, and is endemic to the source. Note that because the 2 source spectra in each epoch were fit simultaneously, they have the same Cash statistic and number of degrees of freedom.

[1] Normalization parameter, where $A = [10^{-14}/(4\pi D^2)] \int n_e n_H dV$, D is the distance to the SMC and the integral is the emission measure.
[2] This value was fixed to be the same abundance as the value in the IKT 18 region.

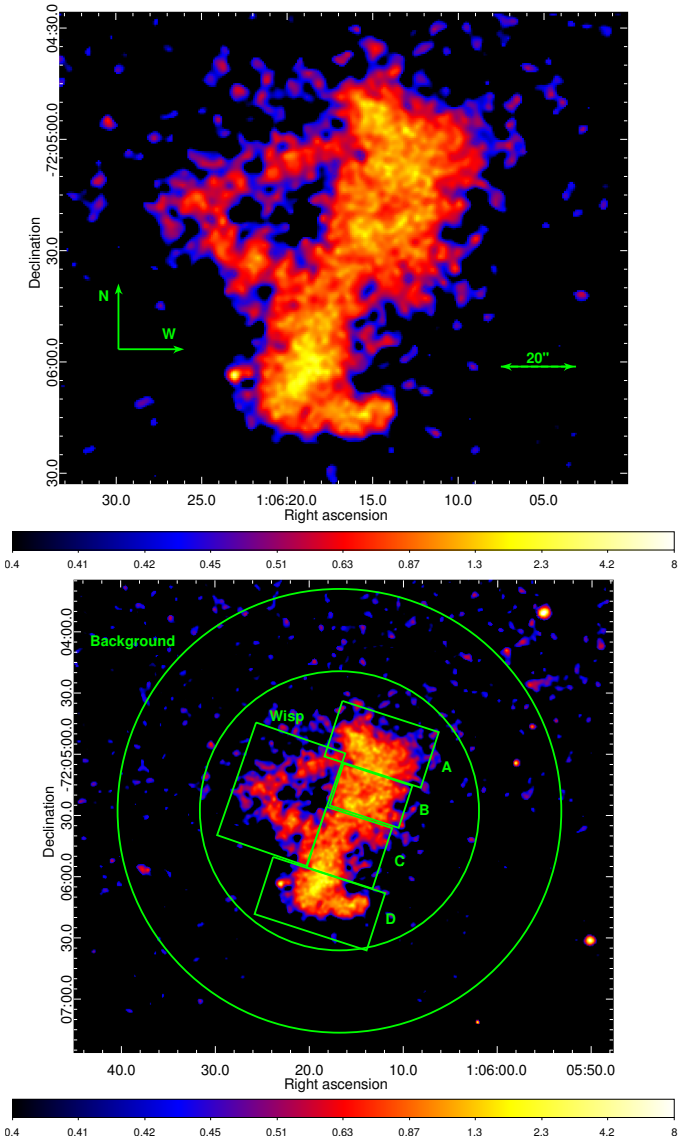

Figure 3.1. The X-ray data of IKT 25. Broadband ACIS images (0.5-8 keV) of IKT 25, binned to the ACIS instrumental resolution (0.5" per pixel), and adaptively smoothed using the *dmimgadapt CIAO* tool, with a kernel of 16 counts over scales from 0.5 pixels to 16 pixels (top), and with spectral extraction regions overlayed (bottom). The colorbar scales are in counts/pixel.

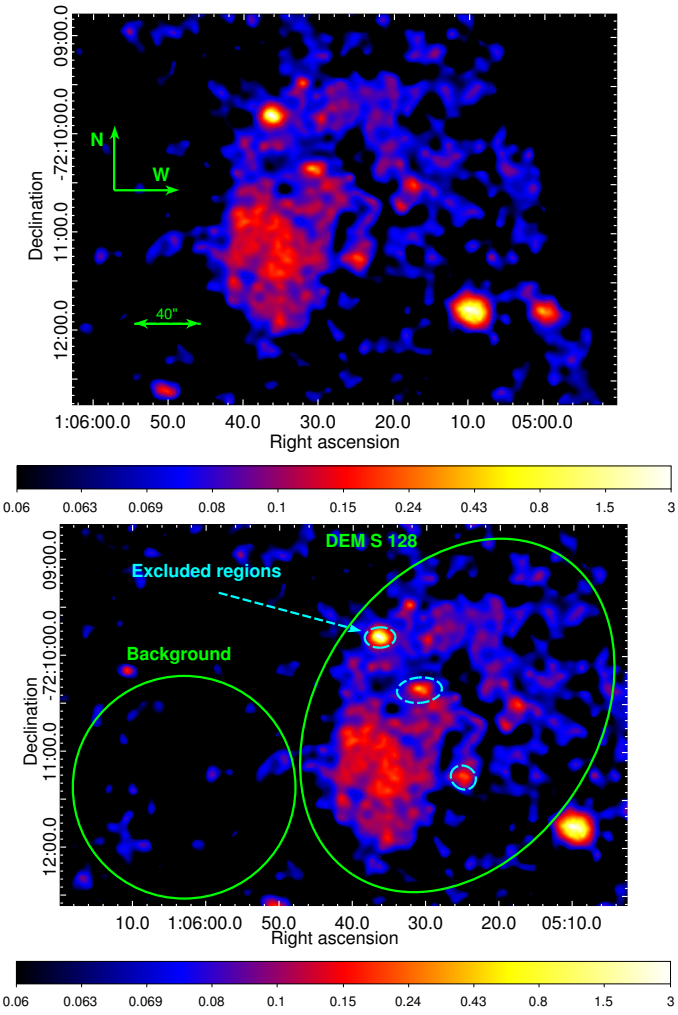

Figure 3.2. X-ray data of DEM S 128. Broadband ACIS images (0.5-8 keV) of DEM S 128 (top), binned to the ACIS instrumental resolution, and adaptively smoothed as in Figure 3.1. The X-ray image of DEM S 128 with spectral extraction regions overlayed (bottom). The colorbar scales of both images are in counts/pixel.

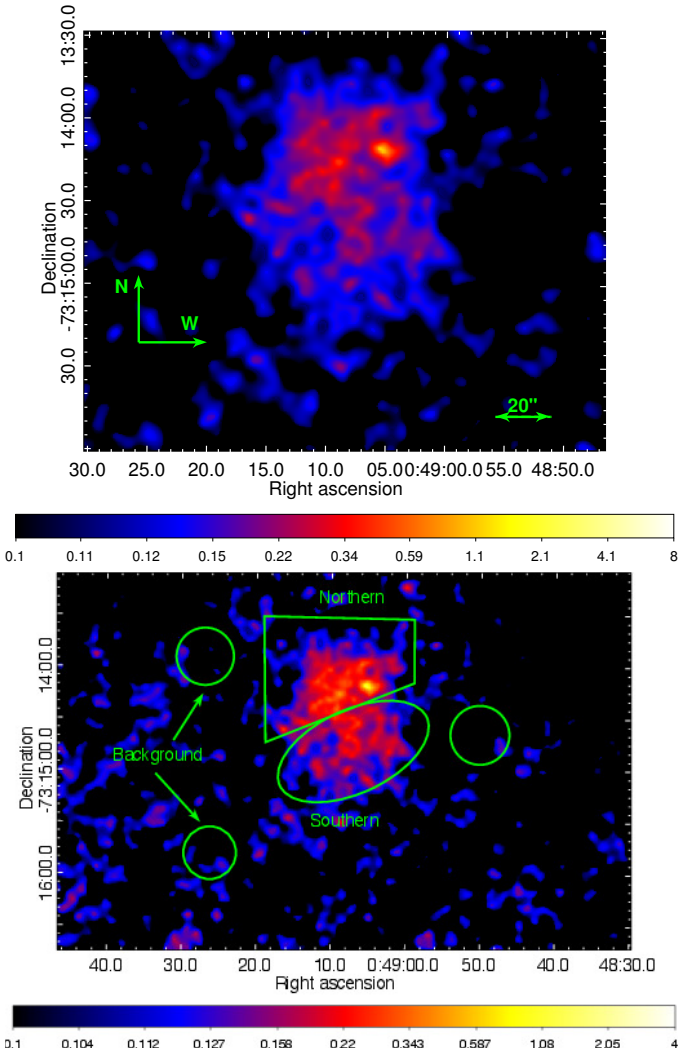

Figure 3.3. The X-ray image of IKT 5. Broadband ACIS images (0.5-8 keV) of IKT 5 (top), binned to the ACIS instrumental resolution, and adaptively smoothed as in Figure 3.1. The X-ray image of IKT 5 with spectral extraction regions overlayed (bottom). The colorbar scales are in counts/pixel.

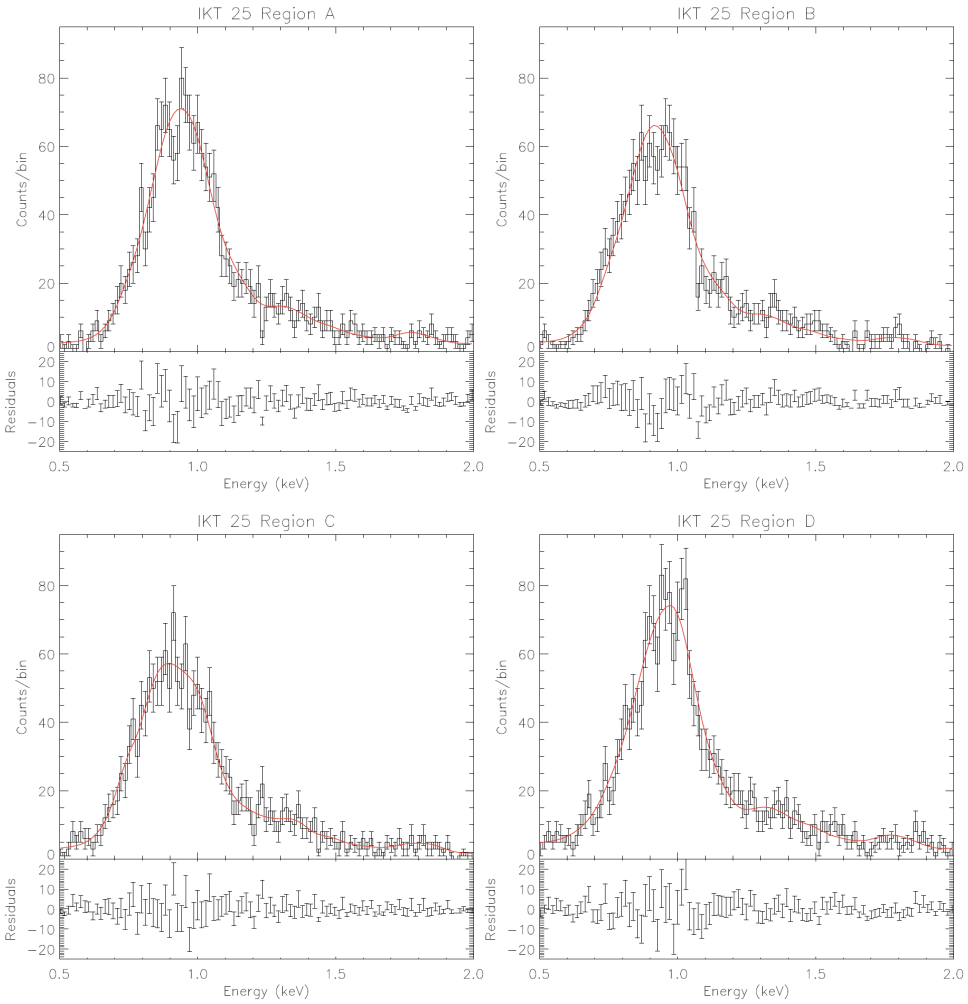

Figure 3.4. The X-ray spectra extracted from IKT 25 from Regions A, B, C and D in Figure 3.1 in black with best fit models corresponding to the best fit model in Figure 3.1 overlayed in red, as well as the residuals of the fit. The uncertainties presented are Poisson, and indicate the 68 % error range to be somewhat analogous to the Gaussian case.

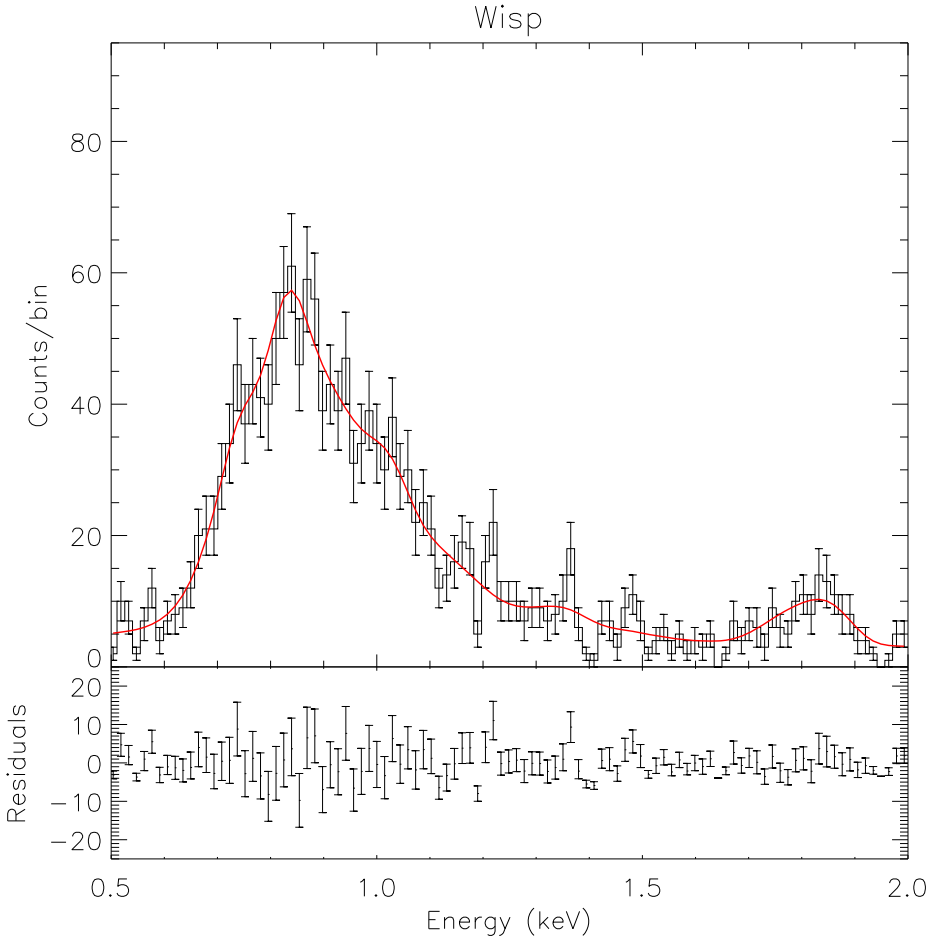

Figure 3.5. The X-ray spectra extracted from IKT 25 from the Wisp region in Figure 3.1 in black with best fit models corresponding to the best fit model in Figure 3.1 overlayed in red, as well as the residuals of the fit. The uncertainties presented are Poisson, and indicate the 68 % error range to be somewhat analogous to the Gaussian case.

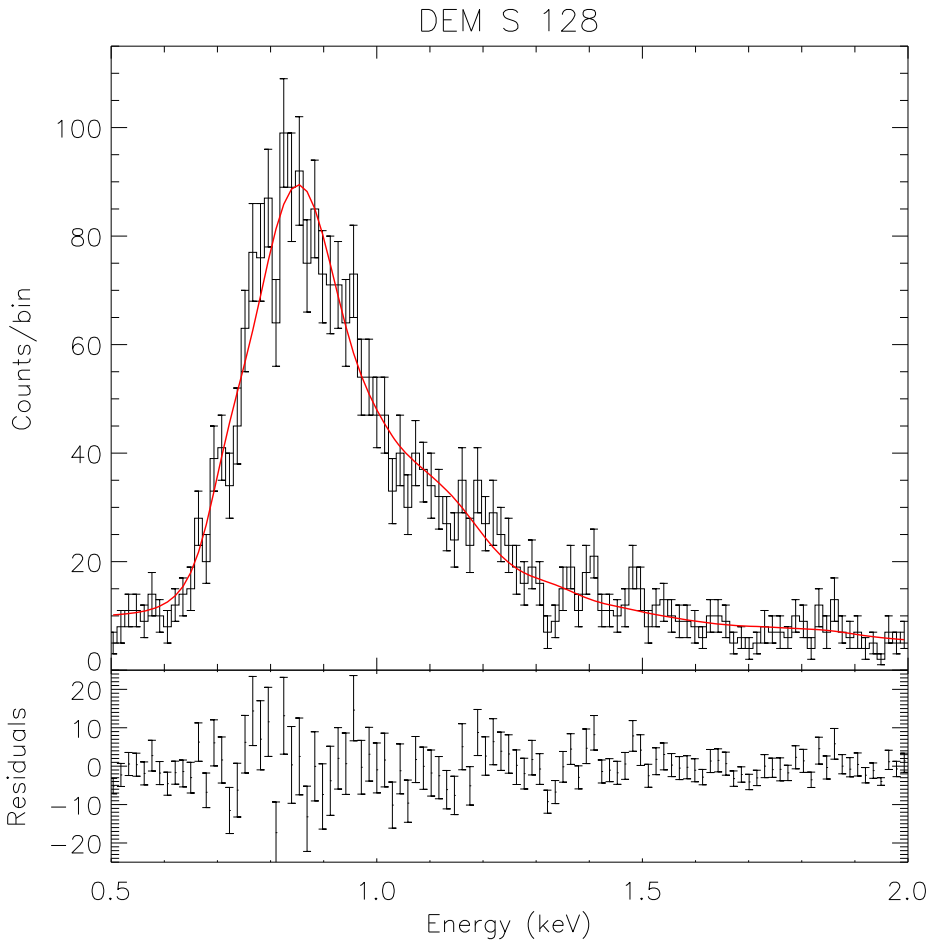

Figure 3.6. The X-ray spectra extracted from DEM S 128 in black with best fit models corresponding to the best fit model overlayed in red. The uncertainties presented are Poisson, and indicate the 68 % error range to be somewhat analogous to the Gaussian case.

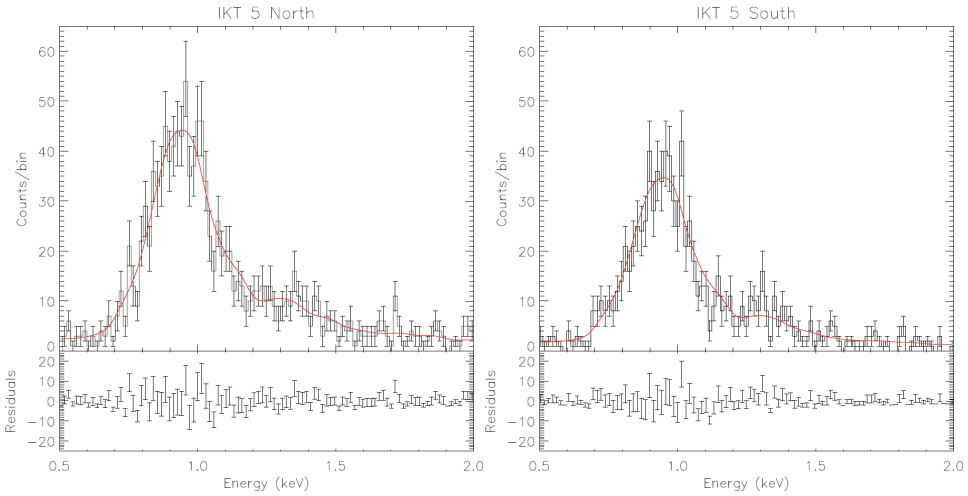

Figure 3.7. The X-ray spectra extracted from IKT 5 in Figure 3.3 in black with best fit models corresponding to the best fit model in Figure 3.3 overlayed in red. They are by region. The uncertainties presented are Poisson, and indicate the 68 % error range to be somewhat analogous to the Gaussian case.

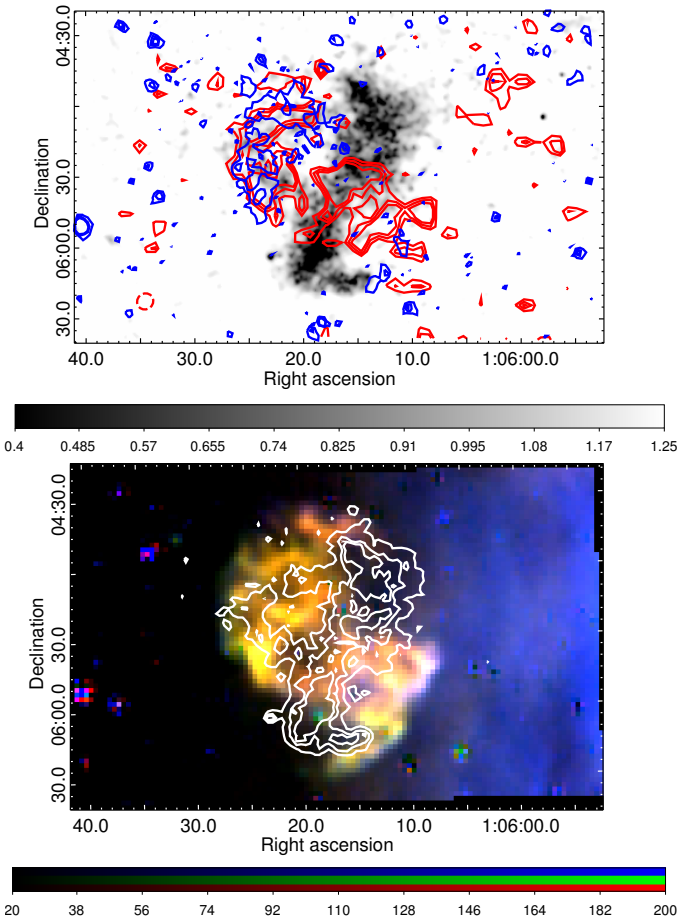

Figure 3.8. IKT 25 in other wavelengths. IKT 25 X-ray data in linear greyscale, with the blue overlayed contours are 8 μm IRAC Spitzer data, and the red overlayed contours are ATCA 20cm flux (top). 8 μm IRAC contours are in units of 0.8, 1.0, and 1.2 MJy/Sr ($\sim$ 4, 5 and 6 σ) while the radio contours are in units of 90, 120 and 150 μJy/beam ($\sim$ 3, 4 and 5 σ). Optical MCELS RGB image of IKT 25, with ACIS contours overlayed (bottom). The red, green and blue are continuum subtracted [S 2], Hα and [O 3], respectively.

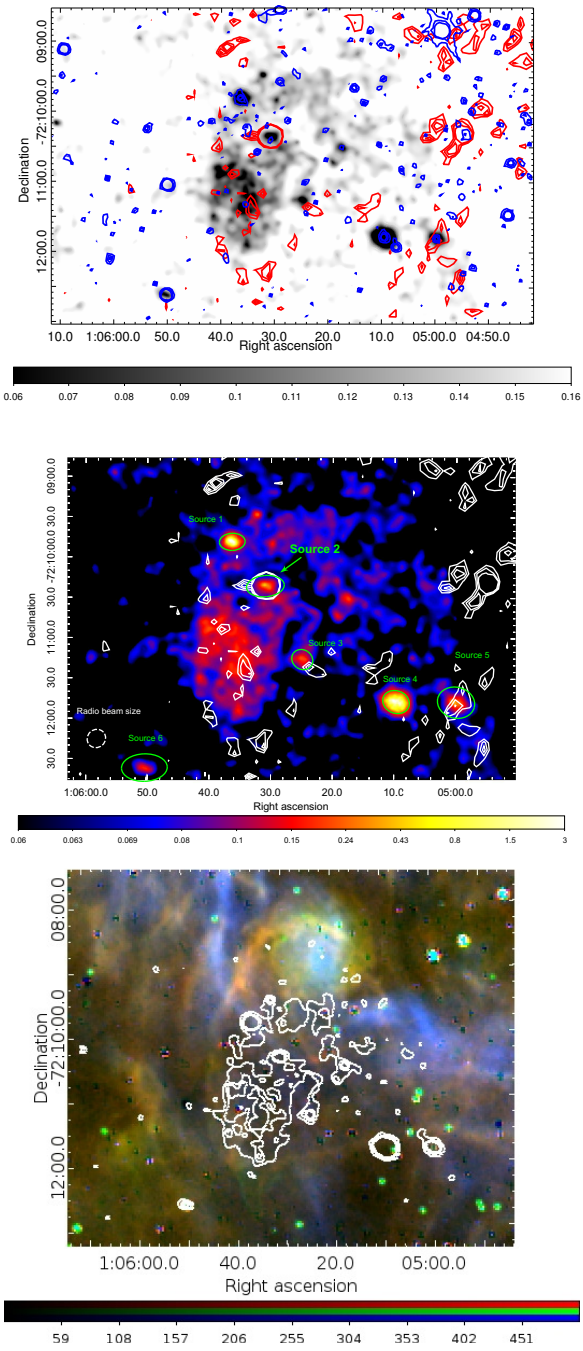

Figure 3.9. DEM S 128 X-ray data in linear greyscale, with the blue overlayed contours are 8 μm IRAC Spitzer data, and the red overlayed contours are ATCA 20cm flux (top). 8 μm IRAC contours are in units of 0.8, 1.0, and 1.2 MJy/Sr ($\sim$ 4, 5 and 6 σ) while the radio contours are in units of 90, 120 and 150 μJy/beam ($\sim$ 3, 4 and 5 σ). DEM S 128 in the ACIS 0.5-2.0 keV waveband in color and 20 cm radio in white contours in units of 90, 120, and 150 μJy (middle). The green regions in the x-ray image are detected point sources, with labels indicating previously detected point sources. Optical MCELS RGB image of DEM S 128, and d. with ACIS contours overlayed (bottom). The red, green and blue are continuum subtracted [S 2], Hα and [O 3], respectively.

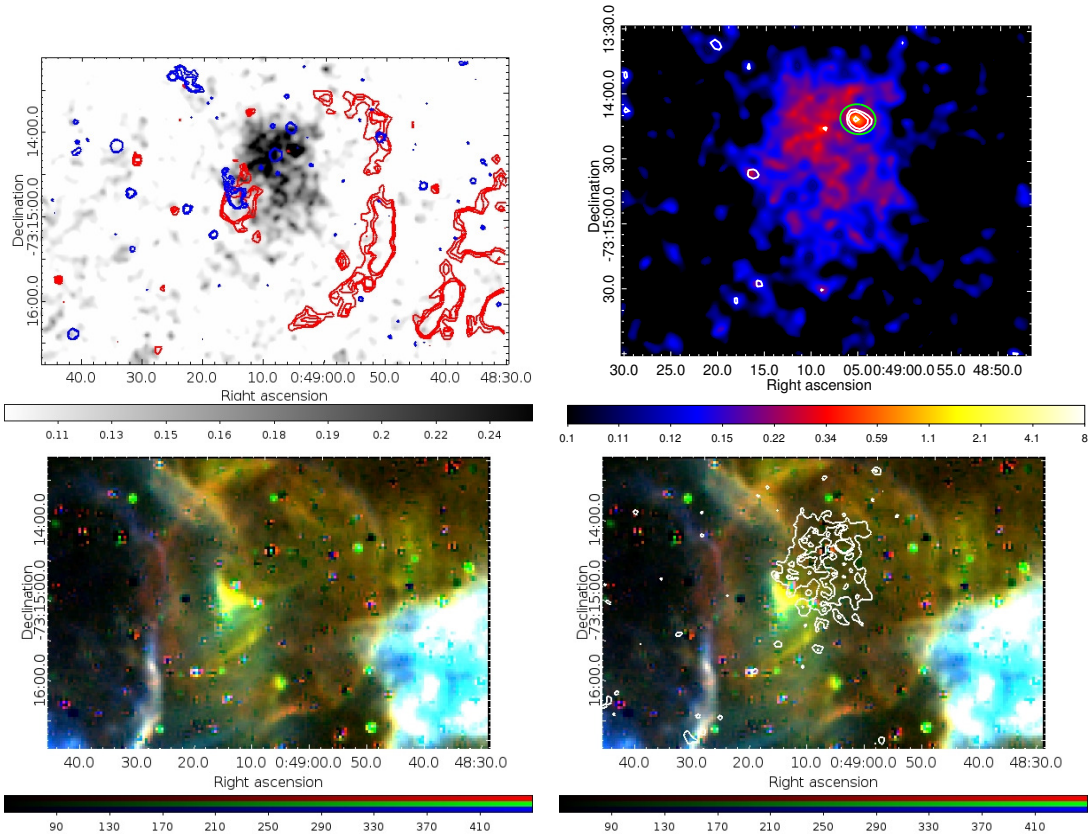

Figure 3.10. IKT 5 data in linear greyscale, with the blue overlayed contours are 8 μm IRAC Spitzer data, and the red overlayed contours are ATCA 20cm flux (upper left). 8 μm IRAC contours are in units of 0.8, 1.0, and 1.2 MJy/Sr ($\sim$ 4, 5 and 6 σ) while the radio contours are in units of 90, 120 and 150 μJy/beam ($\sim$ 3, 4 and 5 σ).The x-ray image are detected point source in white, and green contours in units of 0.12, 0.15, and 0.3 counts/pixel of the ACIS data from 2.0-8.0 keV (upper right). IKT 5 in the ACIS 0.5-2.0 keV waveband in color and 20 cm radio in white contours in units of 90, 120, and 150 μJy (lower left). Optical MCELS RGB image of IKT 5, and with ACIS contours overlayed (lower right). The red, green and blue are continuum subtracted [S 2], Hα and [O 3], respectively.

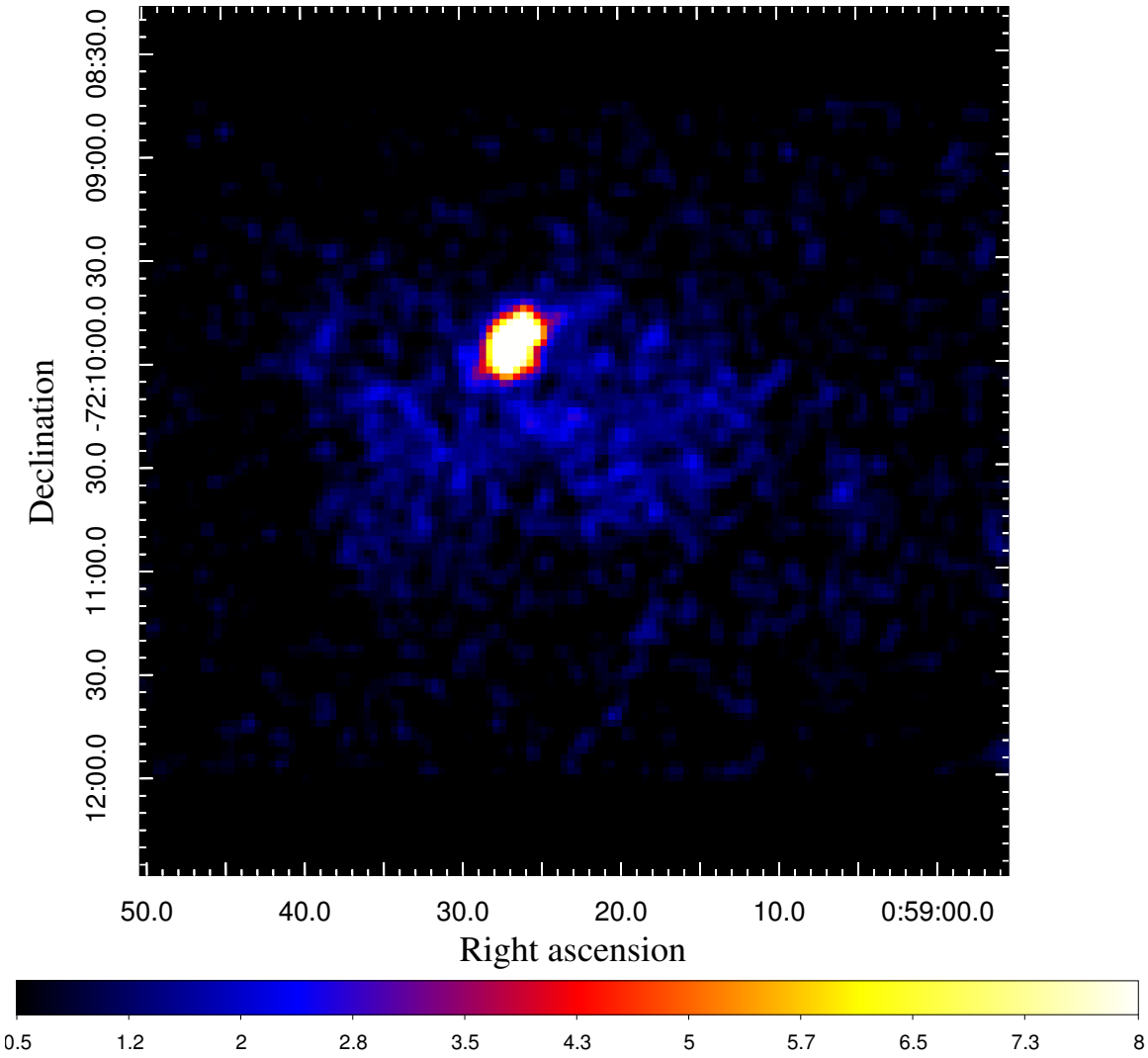

Figure 3.11. The 2013 epoch of X-ray data of IKT 18. the image was binned by a factor of 4 over the ACIS instrumental resolution and smoothed over a gaussian kernal of 2 pixels. The colorbar is in units of counts/pixel.

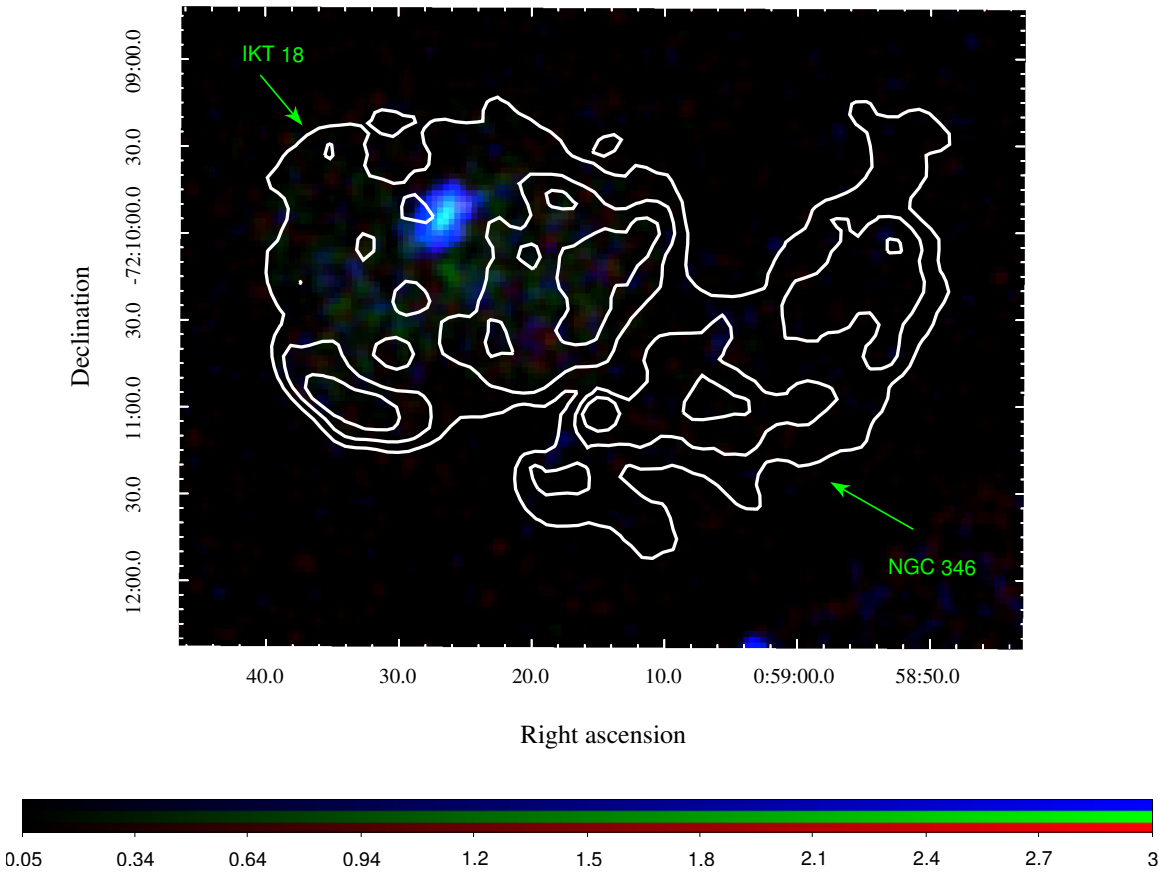

Figure 3.12. The an RGB image of the ACIS-S X-ray data (2013 epoch), smoothed over a kernel of 2 pixels. The red corresponds to the 0.3-0.8 keV band, the green corresponds to the 0.8-1.2 keV energy band, and the blue corresponds to 1.2-8.0 keV. The overlaid contours are ATCA 20cm radio, corresponding to 3, 6, and 9 times the local background. Labelled is the IKT 18 remnant candidate and the NGC 346 SFR.

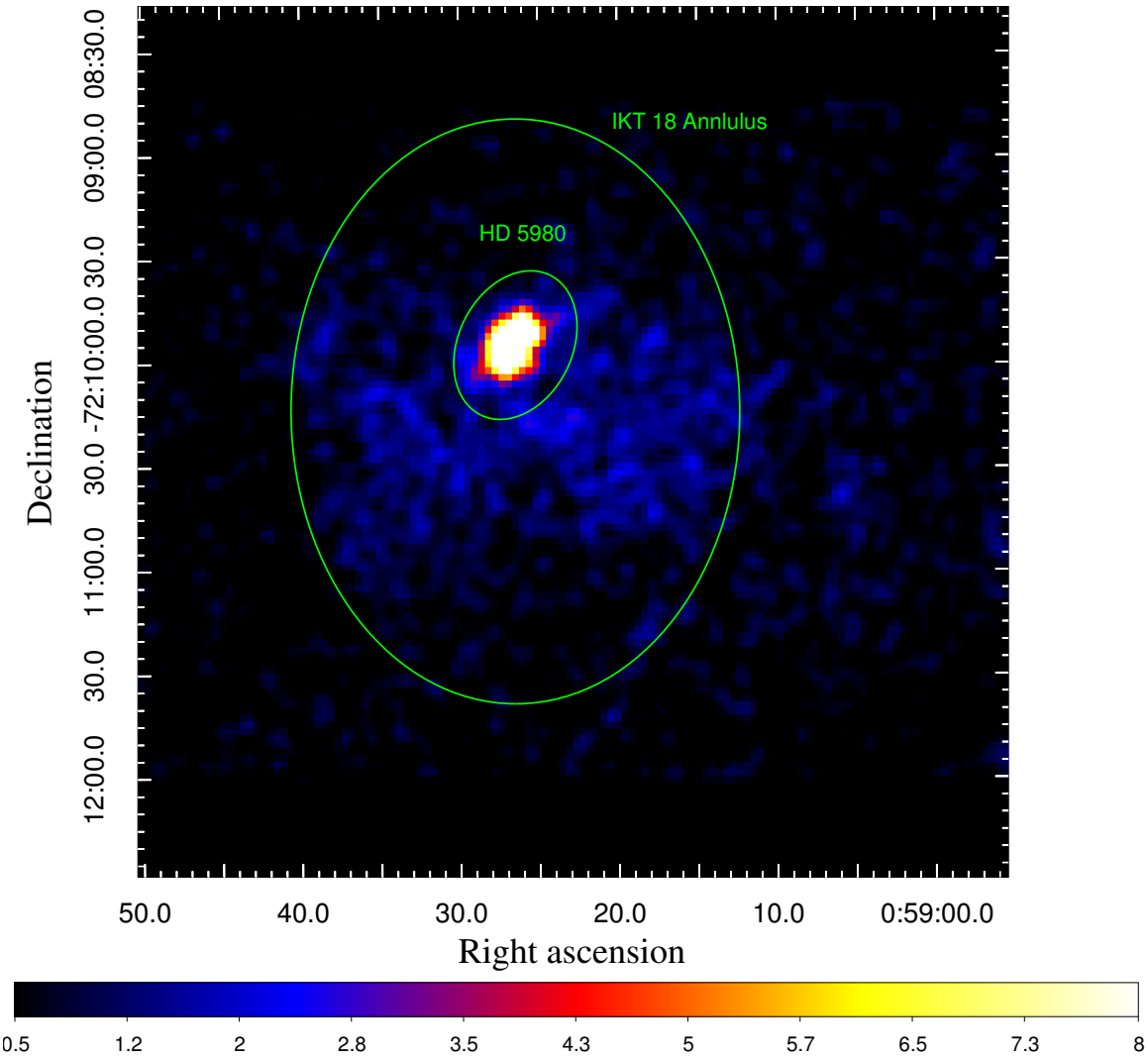

Figure 3.13. The 2013 epoch of X-ray data of IKT 18 in Figure 3.11 with extraction regions overlayed. The point source HD 5980 is excluded from the extraction region of the diffuse IKT 18 region.

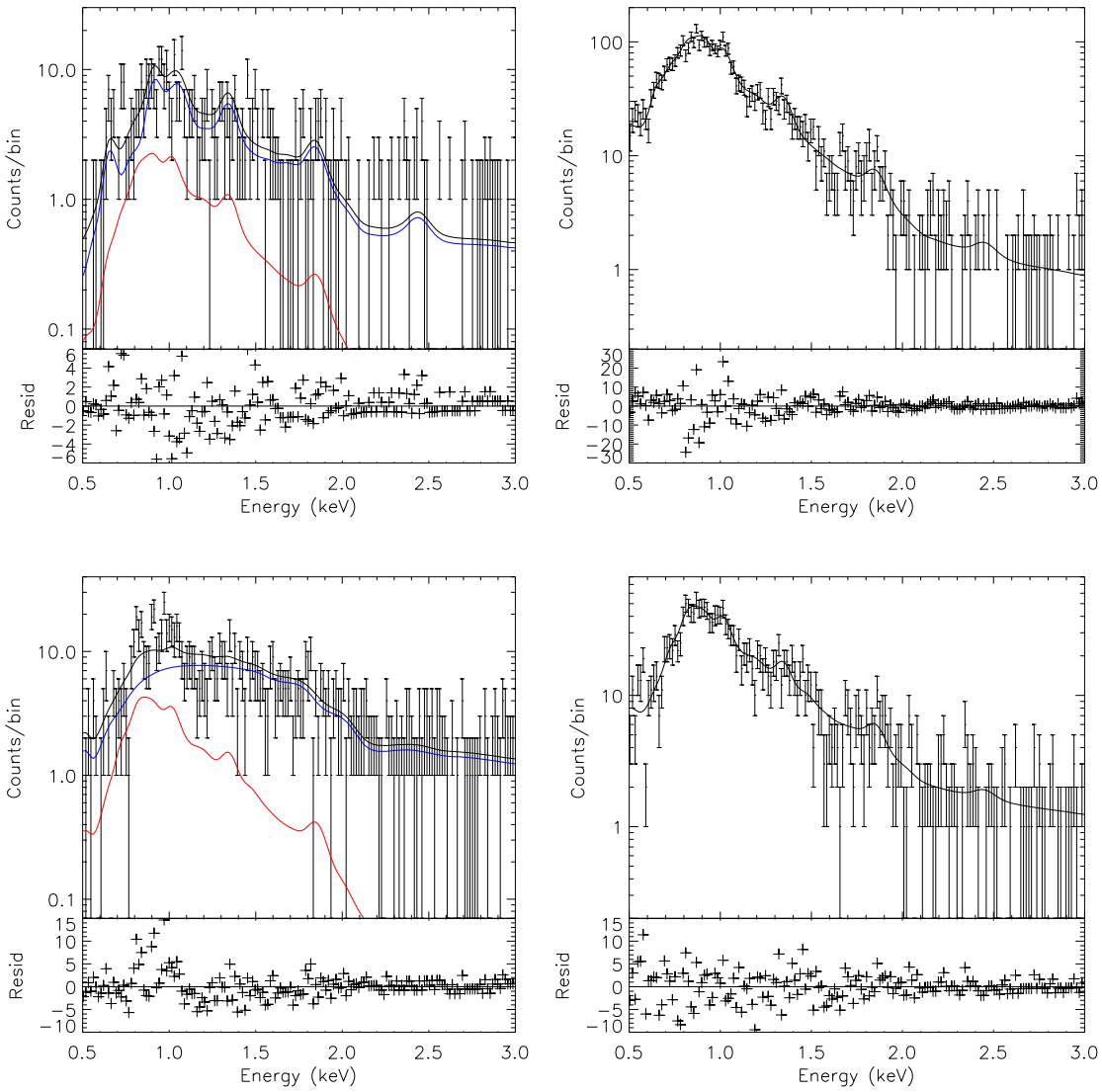

Figure 3.14. The spectra extracted from the regions in Figure 3, with best fit models overlaid. The top row is from the 2001 epoch, with HD 5980 on the left, and IKT 18 on the right. The red curve is the contribution of the IKT 18 plasma in the HD 5980 region, and the blue curve is the HD 5980 source model (with *xspowerlaw* shown).

CHAPTER 4

SUMMARY AND FUTURE WORKS

4.1 Summary

As noted in Chapter 1, Lopez et al. (2011) perform a large census of ejecta-dominated SNRs in the Milky Way and the LMC in which morphology dichotomy which identify Type Ia SNRs as more symmetric, and CC-type SNRs as less symmetric. However, VDH04 also performed a census of SNRs, although in the SMC, in which they identified three Type Ia SNR candidates, IKT 25, DEM S 128, and IKT 5. These remnants are comparatively asymmetric in contrast to the population of CC-type SNRs in the SMC. To resolve this apparent contradiction, I utilize a Poisson PDF analysis and updated plasma models to analyze the X-ray spectrum of these three SNRs. This modelling reveals emission associated with a significant overabundance of iron, which confirms these remnants' status as Type Ia SNRs. However, after augmenting the spectral study with multiwavelength data in the optical, IR and radio, it becomes clear that these remnants are not ordinary Type Ia SNRs. In addition to a much larger-than-expected ionization parameter derived from their X-ray spectra, the multiwavelength investigation revealed that these three remnants were in very complicated environments. This is unusual for Type Ia SNRs, which are thought to arise through very evolved systems. This can be explained if, instead of normal Type Ia SNRs, IKT 25 and IKT 5 are "Prompt" type Ia SNRs, whose progenitor systems are thought to have developed more rapidly than standard Type Ia progenitor systems.

This discovery implies that the environment an SNR expands into plays an important role in the development of its morphology. Moreover, this means that it is not appropriate to apply morphological studies of SNRs like the Lopez study universally. Even though there is value in such morphological studies, there are more complicated SNRs such as IKT 25 that may buck these trends. Our study concludes that ejecta morphology does not always dominate the morphology of SNRs. The environment of SNRs appears to have an effect on their morphology even at ages much younger than the remnants we present in this manuscript. For example, Brantseg et al. (2014) study a plerionic LMC SNR, 0540-69.3, whose age is estimated at 1100 yrs, and find evidence of this remnant's morphology being influenced by local clouds very early in its evolution.

Not only have I characterized three dim SMC SNR, I have strengthened the significance of Fe overabundance from previous studies, which is important. This may not seem important, but as Fe L shell modeling in collisional plasmas is improved, and the amount of Fe L shell line flux increases, the amount of Fe abundance in the model required to fit the same spectrum will decrease. A greater significance of Fe overabudance means a greater confidence that the Fe overabundance is "real", rather than simply due to a lack of atomic knowledge in the model. Furthermore, in this study of IKT 5 and DEM S 128, I utilize X-ray data that have never been analyzed before because of their low signal to noise. This is a direct result of our Poisson likelihood analysis. Low counts data can be handled in a sensible way because there is no requirement about a minimum number of counts per bin.

The updated plasma models I use have updated previous abundance studies. VDH04 lists IKT 25, IKT 5 and DEM S 128 as being overabundant in Ne, which is very unusual for Type Ia remnants. Indeed, this had contributed to the confusion in understanding these three remnants. However, like the problem in the Lopez studies, this can be attributed to the lack of atomic data in the plasma models chosen. Because at the time, the lack of knowledge of Fe-L shell atomic lines in the 0.8-1.0 keV energy band in plasma models at the time, a good model fit to the spectra of these three remnants required an increased flux of Ne-K shell likes in order to "fill in the blank" in the spectrum. While this resulted in a better fit in the VDH04 study, it implied an overabundance of Ne that simply was not present.

I have performed Poisson-PDF X-ray fitting on the SNR IKT 18 and have been able to confirm its identity as a core-collapse SNR. I have ruled out IKT 18 as an LBV nebula due to the LBV-WN binary HD 5980. The amount of time it would have taken a large LBV outburst similar to the outburst of 1994 to form a nebula of the same physical size as IKT 18 is longer than the LBV lifetime. Finally, I have used our Poisson statistical analysis to detect a change in the emission from LBV HD 5980. In 2001, HD 5980 exhibited a hot, line-dominated thermal component. But in the 2013 epoch, I find that the X-ray luminosity of the HD 5980 system has increased by an order of magnitude to a continuum dominated X-ray spectrum. This change in the X-ray emission can be attributed to either an increase in recently shocked, hot thermal plasma, or an increased degree of particle acceleration due in the wind-wind interaction region of HD 5980. In either case, I interpret this change as being due

to the orbital differences between the two epochs due to the system being closer to periastron in the 2013 epoch observation.

Using a Poisson PDF per bin and adopting the Cash statistic is an extremely powerful, general tool. However, it is important to note that using a Poisson PDF statistical analysis is not a good substitute for more data. My analysis has improved upon previous analyses in the low-counts regime, but it is not a panacea that will cure us of the need of higher-quality X-ray data. At some point, we will be limited by resolution and sensitivity of the current X-ray data. That is why upcoming X-ray missions, such as NuSTAR and Astro-H, will be so important as the flagship large observatory X-ray telescopes *Chandra* and *XMM-Newton* are nearing the end of their lives. However, with no replacement large explorer mission capable of imaging spectroscopy in the 0.5-3.0 keV band, improved statistical techniques applied to archival data, such as the one presented in this manuscript will become more and more important in the study of SNR.

As noted in the introduction, the low metallicity of the SMC is a great place to study how SNRs develop in a lower metallicity environment. This is important, because this means that it is more like the early universe than either our galaxy or the LMC. The following section contains several SNR that have archival X-ray data that have not been well-studied due to their low signal to noise, making them ideal candidates to augment the study presented in this manuscript.

4.2 Future Work

4.2.1 IKT 21

IKT 21 is a very compact remnant. IKT 21 is particularly interesting in that a significant portion, roughly 30% of its X-ray emission comes from a point source within the remnant, AX J0103-722 (Hughes & Smith 1994). There are *Chandra* archival data that will be able to potentially resolve the point source seen in the XMM Newton field, and for the first time yield spatial information of the remnant and the point source in its center. The order of magnitude improvement of the angular resolution of *Chandra* over *XMM Newton* will be able to confirm the point source nature of AX J0103-722 and be able to separately extract its spectrum from that of the diffuse emission of the remnant. In addition, our collaborators have obtained ATCA 20 cm radio data of IKT 21 (Figure 4.1). The X-ray point source surrounded by radio emission suggests that this may be a pulsar wind nebula, which could be confirmed with further spectral analysis in both the X-ray and radio data. Further analysis of the radio data external to the X-ray emission will elucidate the morphology of the radio shell. Optical and IR data will also be employed to gain insight into the extant environment of the remnant.

However, the point source in IKT 21 is very variable in the X-ray. The *Chandra* ACIS data shows that the point source AX J0103-722 is highly variable, as can be seen in Figure 4.2. This object is near IKT 22, the brightest SNR in the SMC, which is a standard extragalactic source calibrator for *Chandra*. Because of this, there is quite a bit of data, ~ 200 *ksec* in total, in which IKT 21 is serendipitously detected.

However, many of these observations are in short, 5-10 *ksec* calibration observations across many different parts of the *ACIS* CCDs. Because of this, combining the spectra extracted from all these observations and performing a standard Gaussian-PDF analysis would be difficult. However, simultaneous spectral fitting each of the dozens of independent low counts spectra extracted using my Poisson-PDF analysis technique, as I have done in the IKT 18/HD 5980 observation, is relatively straightforward, if computationally arduous. Using this technique, we may be able to characterize the diffuse emission surrounding IKT 21 in those observations where AX J0103-722 is X-ray quiet, as well as gaining new insight into AX J0103-722 when it is detectable.

4.2.2 IKT 16

Owen et al. (2011) looked at this remnant in detail. They used *XMM-Newton's EPIC* and *MOS* detectors, depicted in Figure 4.3 to examine the X-ray structure of IKT 16. They report that its dynamical age is 14,700 years, which puts it at roughly the same age as DEM S 128. Their data show a central point source with surrounding diffuse emission. Similar to IKT 21, we will use *Chandra* in order to confirm the unresolved nature of this source and further isolate its emission in spectral analysis from its surrounding diffuse emission. Inclusion of MCELS, Spitzer, and new radio data will reveal possible environmentally induced morphology of this remnant.

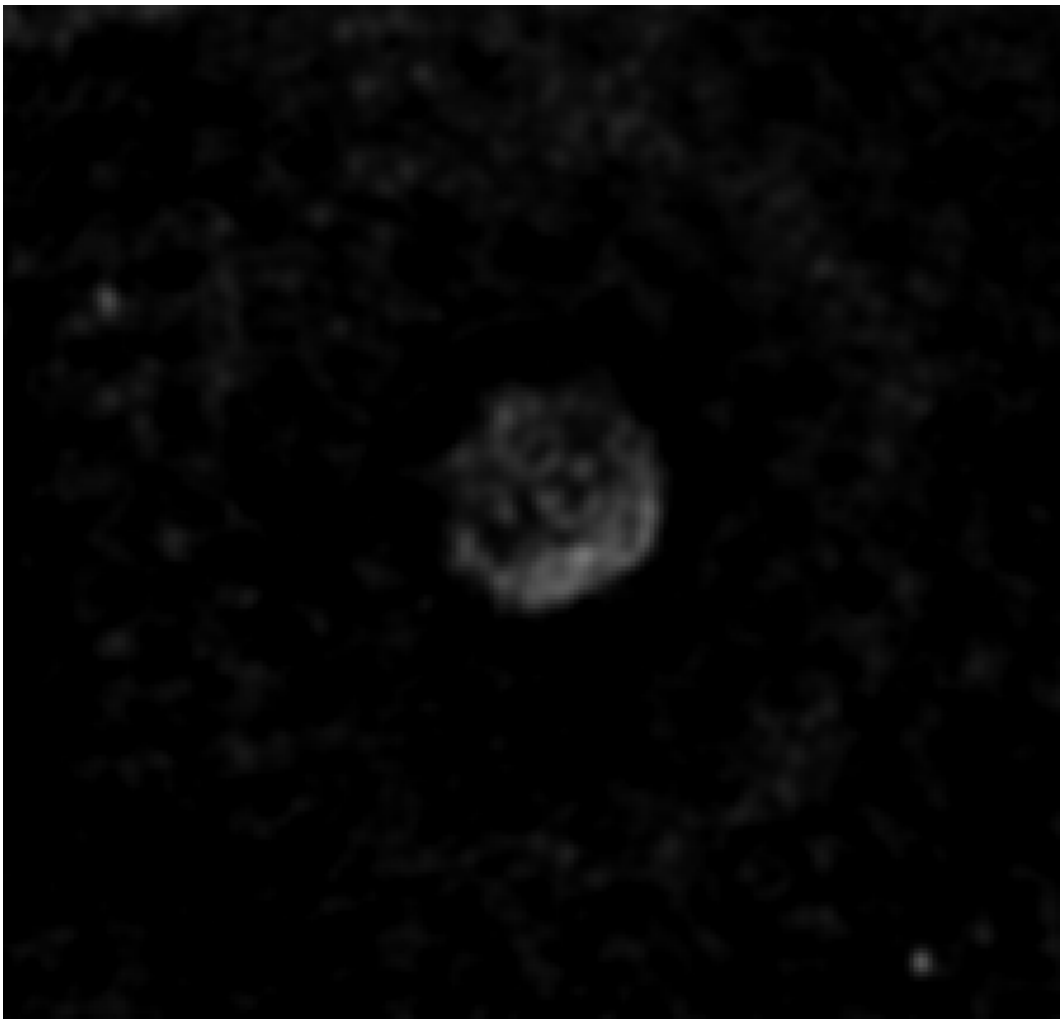

Figure 4.1. ATCA 20 cm radio image of IKT 21. The increased radio flux towards the southwest of the remanant suggests potential limb-brightening.

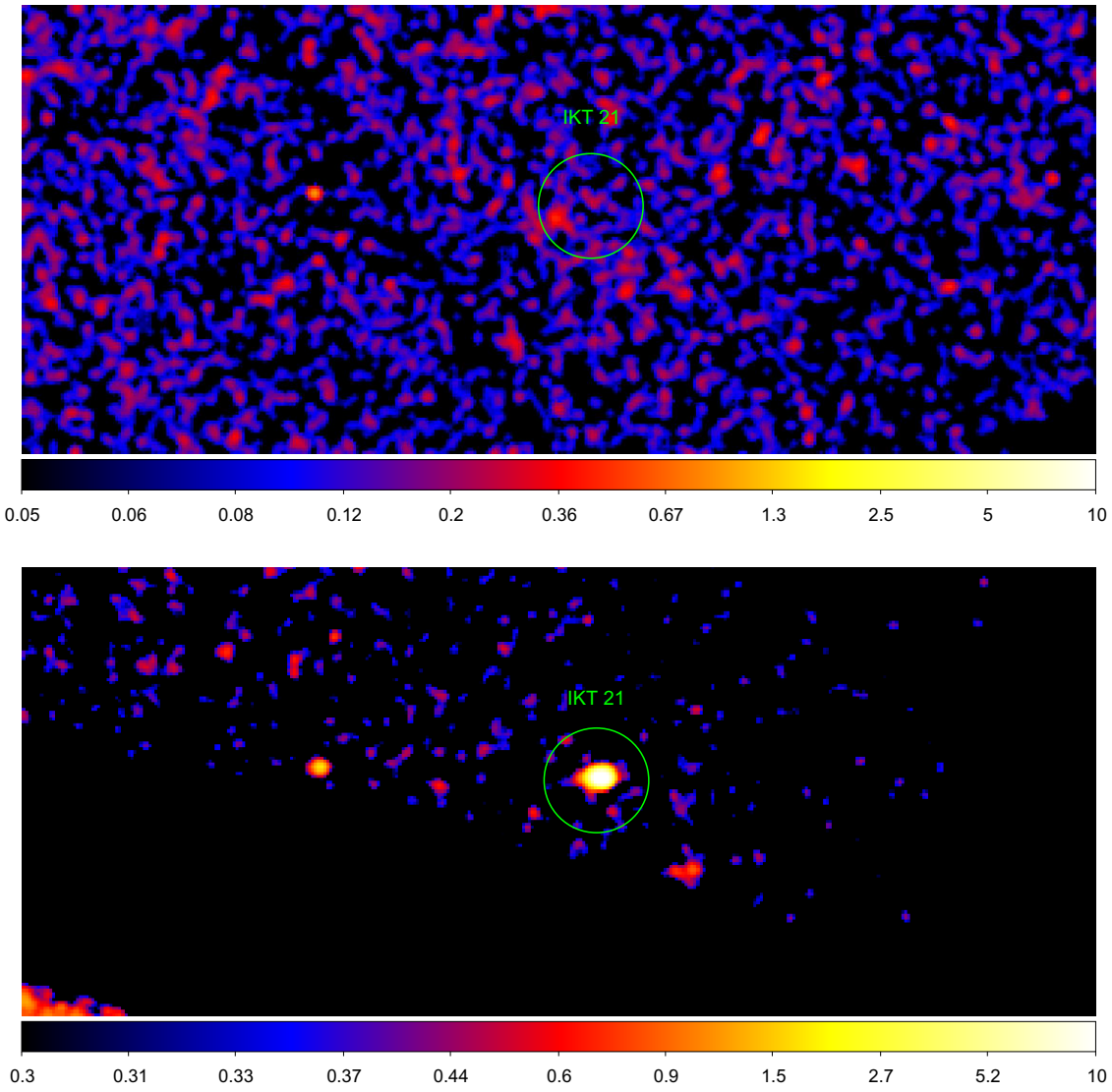

Figure 4.2. Two X-ray images of IKT 21 with similar exposure times taken a couple of years apart. Note that in the top panel, the lower threshold of the color bar is nearly the average background counts. In the top panel, we do not see AX J0103-722, but in the bottom panel it is clearly visible.

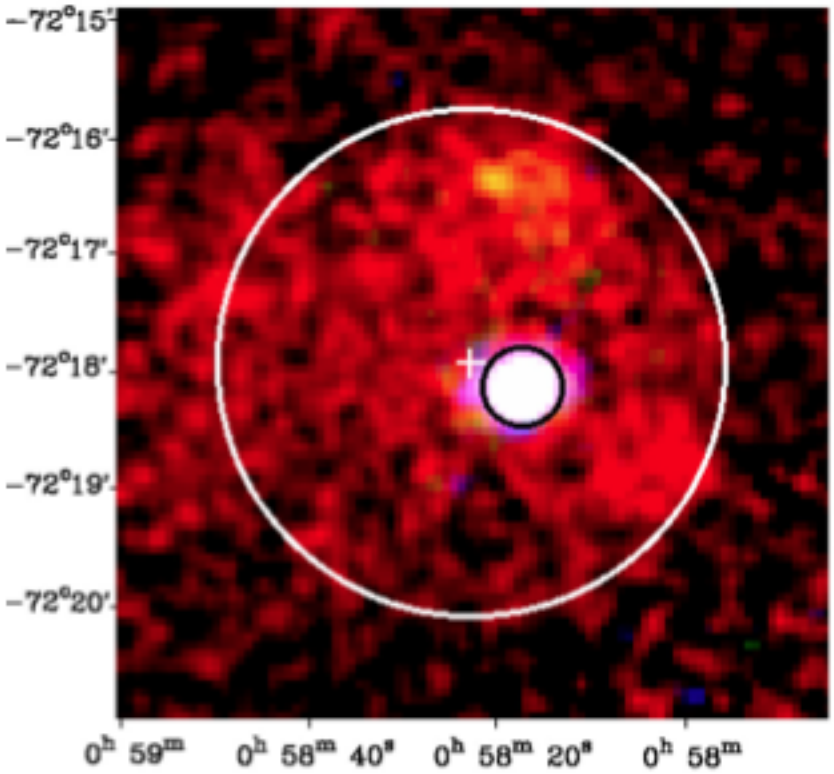

Figure 4.3. The SNR IKT 16 in three colors as detected by *XMM-Newton's* EPIC detector. Notice the unresolved source in the center of the remnant whose spectrum is harder than the rest of the remnant.

REFERENCES

Barba, R., Morrell, N., Niemela, V., et al. 1996, in Revista Mexicana de Astronomia y Astrofisica, vol. 27, Vol. 4, Revista Mexicana de Astronomia y Astrofisica Conference Series, ed. E. Falco, J. A. Fernandez, & R. F. Ferrero, 90

Borkowski, K. J., Hendrick, S. P., & Reynolds, S. P. 2006, ApJ, 652, 1259

Brantseg, T., McEntaffer, R. L., Bozzetto, L. M., Filipovic, M., & Grieves, N. 2014, ApJ, 780, 50

Breysacher, J., & Perrier, C. 1980, A&A, 90, 207

Brickhouse, N., Cowan, J., Drake, P., et al. 2009, in Astronomy, Vol. 2010, astro2010: The Astronomy and Astrophysics Decadal Survey, 68P

Chevalier, R. A. 1982, ApJ, 258, 790

—. 2005, ApJ, 619, 839

Chu, Y.-H., Gruendl, R. A., Stockdale, C. J., et al. 2004, AJ, 127, 2850

Churazov, E., Gilfanov, M., Forman, W., & Jones, C. 1996, ApJ, 471, 673

Corcoran, M. F., Ishibashi, K., Swank, J. H., & Petre, R. 2001, in Astronomical Society of the Pacific Conference Series, Vol. 233, P Cygni 2000: 400 Years of Progress, ed. M. de Groot & C. Sterken, 75

Da Silva, L. 1993, Astrophysics and Space Science, 202, 215

Davies, R. D., Elliott, K. H., & Meaburn, J. 1976, MmRAS, 81, 89

Dickey, J. M., & Lockman, F. J. 1990, ARA&A, 28, 215

Draine, B. T. 2011, Physics of the Interstellar and Intergalactic Medium

Filipović, M. D., Haberl, F., Pietsch, W., & Morgan, D. H. 2000, A&A, 353, 129

Filipović, M. D., Payne, J. L., Reid, W., et al. 2005, MNRAS, 364, 217

Flanagan, K. A., Canizares, C. R., Dewey, D., et al. 2004, ApJ, 605, 230

Foellmi, C., Koenigsberger, G., Georgiev, L., et al. 2008, Rev. Mexicana Astron. Astrofis., 44, 3

Fruscione, A., McDowell, J. C., Allen, G. E., et al. 2006, in Society of Photo-Optical Instrumentation Engineers (SPIE) Conference Series, Vol. 6270, Society of Photo-Optical Instrumentation Engineers (SPIE) Conference Series

Georgiev, L., Koenigsberger, G., Hillier, D. J., et al. 2011, AJ, 142, 191

Hamaguchi, K., Corcoran, M. F., Russell, C. M. P., et al. 2014, ApJ, 784, 125

Hilditch, R. W., Howarth, I. D., & Harries, T. J. 2005, MNRAS, 357, 304

Hughes, J. P., & Helfand, D. J. 1985, ApJ, 291, 544

Hughes, J. P., & Smith, R. C. 1994, AJ, 107, 1363

Humphreys, R. M. 1991, in IAU Symposium, Vol. 143, Wolf-Rayet Stars and Interrelations with Other Massive Stars in Galaxies, ed. K. A. van der Hucht & B. Hidayat, 485

Inoue, H., Koyama, K., & Tanaka, Y. 1983, in IAU Symposium, Vol. 101, Supernova Remnants and their X-ray Emission, ed. J. Danziger & P. Gorenstein, 535–540

Ishibashi, K., Corcoran, M. F., Davidson, K., et al. 1999, ApJ, 524, 983

Koenigsberger, G., Georgiev, L., Barbá, R., et al. 2000, ApJ, 542, 428

Koenigsberger, G., Georgiev, L., Hillier, D. J., et al. 2010, AJ, 139, 2600

Koyama, K., Petre, R., Gotthelf, E. V., et al. 1995, Nature, 378, 255

Laycock, S., Zezas, A., Hong, J., Drake, J. J., & Antoniou, V. 2010, ApJ, 716, 1217

Lee, J.-J., Park, S., Hughes, J. P., Slane, P. O., & Burrows, D. N. 2011, ApJ, 731, L8

Leyder, J.-C., Walter, R., & Rauw, G. 2010, A&A, 524, A59

Lopez, L. A., Ramirez-Ruiz, E., Huppenkothen, D., Badenes, C., & Pooley, D. A. 2011, ApJ, 732, 114

Massey, P. 2003, ARA&A, 41, 15

Massey, P., & Olsen, K. A. G. 2003, AJ, 126, 2867

Nazé, Y., Hartwell, J. M., Stevens, I. R., et al. 2002, ApJ, 580, 225

Ohnishi, T., Uchida, H., Tsuru, T. G., et al. 2014, ApJ, 784, 74

Owen, R. A., Filipović, M. D., Ballet, J., et al. 2011, A&A, 530, A132

Payne, J. L., White, G. L., Filipović, M. D., & Pannuti, T. G. 2007, MNRAS, 376, 1793

Reynolds, S. P. 2008, Annu. Rev. Astron. Astrophys., 46, 89

Russell, S. C., & Dopita, M. A. 1992, ApJ, 384, 508

Sault, R. J., Teuben, P. J., & Wright, M. C. H. 1995, in Astronomical Society of the Pacific Conference Series, Vol. 77, Astronomical Data Analysis Software and Systems IV, ed. R. A. Shaw, H. E. Payne, & J. J. E. Hayes, 433

Smartt, S. J. 2009, ARA&A, 47, 63

Spitzer, L. 1998, Physical Processes in the Interstellar Medium

Truelove, J. K., & McKee, C. F. 1999, ApJS, 120, 299

van der Heyden, K. J., Bleeker, J. A. M., & Kaastra, J. S. 2004, A&A, 421, 1031

Ye, T., & Turtle, A. J. 1991, MNRAS, 249, 693